Materials Chemistry and Physics 348 (2026) 131566

Contents lists available at ScienceDirect

Materials Chemistry and Physics

journal homepage: www.elsevier.com/locate/matchemphys

Tailoring graphitic carbon nitride for ultracapacitor electrode application through nanocompositing with SnO_2 and WO_3

Peter Kganyago [a,b], Messai Mamo [a], Edwin T. Mombeshora [b], Patrick G. Ndungu [b,*]

[a] Department of Chemical Sciences, University of Johannesburg, P.O. Box 17011, Doornfontein, Johannesburg, 2028, South Africa
[b] Department of Chemistry, University of Pretoria, Private Bag X20, Hatfield, 0028, South Africa

HIGHLIGHTS

- Pristine g-C_3N_4 has low electro-active surfaces and poor electronic conductivity.
- Electrode characteristics improved by binary and ternary nanocomposites synthesis.
- Aim was hydrothermal synthesis of g-C_3N_4 nanocomposites with SnO_2 and WO_3.
- Morphology, electro-active surfaces, and capacitive traits tuned in nanocomposites.
- SnO_2-WO_3-g-C_3N_4 nanocomposite displayed the highest improvement in capacitance.

GRAPHICAL ABSTRACT

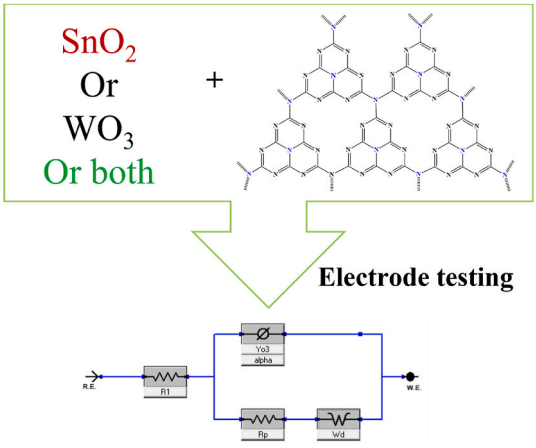

ARTICLE INFO

Keywords:
Electrochemical capacitor
Carbon
Energy storage
Ternary
Graphene

ABSTRACT

Supercapacitors are a promising and necessary pillar that can aid the full-fledged adoption of intermittent renewable energy resources and emerging portable technologies. The performance of supercapacitors largely depends on the physicochemical properties of the electrode materials, which are centred on design and composition. The g-C_3N_4, as a 2D graphitic material, has long been recognised as a suitable electrode material for supercapacitors due to readily available sources. However, limited electro-active surfaces and low conductivities have posed significant challenges. Modifying physicochemical properties through compositing has emerged as a suitable approach to enhance their applicability in energy storage by generating hybrid electrode types. In this context, the current work investigated SnO_2 nanoparticles and WO_3 nanorods as enhancers of g-C_3N_4 nanosheets in binary (WO_3-g-C_3N_4 and SnO_2-g-C_3N_4) and ternary (SnO_2-WO_3-g-C_3N_4) nanocomposites for applications in supercapacitor electrodes. Properties were synergistically tailored; for instance, charge transfer resistance of SnO_2-WO_3-g-C_3N_4, g-C_3N_4, SnO_2-g-C_3N_4, and WO_3-g-C_3N_4 were 1.55, 1.26, 0.8 and 0.48 Ω, respectively. Consequently, incorporation of SnO_2 and WO_3 amplified energy storage by 119% and 172% in binary nanocomposites, while the ternary nanocomposites showed an improvement of 192%. The SnO_2-g-C_3N_4, WO_3-g-C_3N_4

* Corresponding author.
E-mail address: patrick.ndungu@up.ac.za (P.G. Ndungu).

https://doi.org/10.1016/j.matchemphys.2025.131566
Received 13 June 2025; Received in revised form 1 September 2025; Accepted 17 September 2025
Available online 18 September 2025

and SnO_2-WO_3-g-C_3N_4 materials attained cycle stability of 70, 96, and 50%, respectively, after 2000 cycles. Other key synergism attributes from the work include morphological transformations that enhanced structural rigidity, intimate connectivity through chemical linkages, improved electro-active surfaces, and additional pseudo-capacitive contributions in the nanocomposites. The studied nanocomposites highlight that g-C_3N_4 can be favourably tuned in this manner and pave the way for significant potential in sustainable electrodes for abundant, clean, and renewable electrochemical energy.

1. Introduction

Worldwide population growth, industrialisation, and economic advances, projecting a doubling of energy requirements by 2050 [1], have led to the need for progress not only in sustainable energy resources but also in energy materials. Moreover, the intermittent nature of most renewables makes them vulnerable to effective and sustainable energy storage needs [2]. In an attempt to mitigate this, *2D* carbon nanomaterials have received significant attention for innumerable energy applications because of their attractive attributes. For example, owing to viable and tailorable physicochemical and electrochemical attributes, graphitic carbon nitride (g-C_3N_4) is an example of a versatile and hotspot *2D* material that can complement graphene in being applicable in wide-ranging energy applications, such as batteries, fuel cells, hydrogen production, solar cells, and supercapacitors [3].

On this list of possibilities, supercapacitors are striking for their fast charge/discharge times (a few seconds), high power density ($\leq 10^3$ kW kg^{-1}), longer life-span ($\approx$10 years at room temperature) and commendable cycle life ($>10^6$ charge-discharge cycles) [4–6]. However, supercapacitors still have lower energy density and a smaller global market share than conventional batteries [7,8]. Adding to the current concerns of supercapacitors, most carbonaceous materials, such as graphene derivatives and g-C_3N_4, are still far below their theoretical specific capacitance (C_s) values ($\approx$200 F g^{-1}) [9,10]. Hence, there is a need to advance their performance when their other merits are considered. One active route is through designing hybrid supercapacitors that combine the merits of electrochemical double-layer capacitors (EDLC) and pseudo-capacitors [11].

The allure of g-C_3N_4 encompasses environmental friendliness, its classification as "*earth-abundant*," thermal and chemical stability, a nitrogen-rich backbone, and a straightforward synthesis protocol [1,12]. The g-C_3N_4 is primarily synthesised from nitrogen-rich precursors, commonly melamine and urea, *via* pyrolysis at temperatures exceeding 400 °C [13]. Unlike graphene, g-C_3N_4 features three carbon atoms in the graphitic framework replaced by nitrogen atoms. The aromatic tri-s-triazine moieties of g-C_3N_4 render it an appealing alternative material for the energy storage sector and have recently garnered attention for supercapacitor applications [3]. The presence of nitrogen functionalities within the π-conjugated graphite planes is crucial for increasing the number of electro-active sites by contributing additional pseudo capacitance, improving electron transport efficiency and wettability in electrolytes [1,3]. Despite the promising nitrogen moieties in the graphitic backbone, among other characteristics, the use of g-C_3N_4 in supercapacitors is presently impeded by low electro-active surfaces and poor electronic conductivity due to its properties as a large band gap semiconductor (2.7 eV) [3,14,15]. This necessitates a search for methods to enhance energy storage performance. The electrochemical energy storage characteristics of g-C_3N_4 can be optimised by adjusting conductivity, pore structure and morphology through composite synthesis [14]. In this regard, one potential method for improving the electrochemical performance of the g-C_3N_4 nanomaterial involves the incorporation of nano-structured transition metal oxides (TMOs) for synergistic performance. Nano-structural manipulation optimally allows for the adjustment of the surface-volume ratio, which is ideal for increasing surface energy storage and facilitating quantum confinement essential for modulating charge transport and electronic band structure [10,16].

One lucrative TMO for this role is WO_3 and is under focus for supercapacitor applications because of its high abundance, nanostructural nature, corrosion resistance, electrochemical stability, cost-effectiveness and high theoretical C_s of 1112 F g^{-1} [16–19]. For example, WO_3-multiwalled carbon nanotube (MWCNT) binary nanocomposites on carbon cloth were applied as supercapacitor electrodes and an optimum C_s of 276% that of WO_3 with a C_s retention of 94% after 5000 cycles in 1 M $LiClO_4$ electrolyte was reported [20]. Furthermore, the WO_3-MWCNT binary nanocomposite-based electrode from their work had longer discharge periods than the electrodes made from individual WO_3 and MWCNT. WO_3-based electrodes are also being advanced for photo-assisted supercapacitor applications. To illustrate this, C_s of the WO_3-MWCNT binary nanocomposite-based electrode were $\approx$127 % and 259% higher than those of electrodes from WO_3 and MWCNT, respectively [19]. This was attributed to fast charge transports and easier intercalation of electrolyte ions owing to improved electro-active surface area. Porosity enhancement through composites is another strategy reported for improving the C_s of carbonaceous materials. For illustration, porous MWCNTs-WO_3-graphite nanocomposite-based electrode in 1 M H_2SO_4 electrolyte was improved by $\approx$170% from that of the non-porous nanocomposite [18]. Also, MnO_2-porous carbon electrodes in 1 M Na_2SO_4 electrolyte with a specific surface area of 2250 m^2 g^{-1} improved the C_s by threefold from that of porous carbon alone [21]. However, the optimum cycle stability of MnO_2-porous composite (75%) after 1000 cycles was lower and higher than that of electrodes of porous carbon (90%) and MnO_2 (50%), respectively. This is another interesting manifestation of how composites can result in different impacts on the components owing to the possibility of the existence of either a physical or chemical composite structure.

Additional studies involving carbonaceous composites as electrodes include a *3D* network of hexagonal WO_3-rGO nanocomposites in 1 M H_2SO_4 electrolyte with $\approx$170% and 93% C_s and C_s retention after 2000 cycles when compared to that of WO_3 electrodes [17]. Another similar study utilised WO_3-rGO nanocomposites on supercapacitor electrodes in 1 M H_2SO_4 electrolyte, and the reported champion C_s was 559% that of GO and WO_3 electrodes with 87% C_s retention after 5000 cycles [22]. A WO_3-WS_2-MWCNTs ternary nanocomposite on a Ni foam electrode attained a larger integrated area under the voltammograms than the individual components and culminated in $\approx$127% and 270% of WO_3-WS_2 binary composite and WO_3, respectively, in 3 M KOH electrolyte, thus, indicative of significant improvements in composites [23]. An electrode based on *monoclinic*-WO_3-$Ti_3C_2T_X$-hollow graphene foam in 1 M H_2SO_4 electrolyte recorded a C_s improvement of 138% from that of *monoclinic*-WO_3-hollow graphene binary composite and cycle stability and 93% after 5000 cycles, respectively [24]. From the reviewed recent studies, it is clear that acidic electrolytes have been mostly used, and WO_3 is suitable for improving energy storage applications of carbonaceous materials. Though with few reports with high cycle stability emerging, major malfunctions of TMOs, such as WO_3, are maintaining optimum C_s during charge/discharge cycles, poor rate performance and cycle performance due to poor conductivity [19,25]. There is a current drive to develop composites of WO_3 for supercapacitor applications, and there are a few composites, if not any, that involve WO_3 and g-C_3N_4 for supercapacitor applications.

Another potential TMO supercapacitor electrode material is SnO_2 because of its suitability in electron mobility characteristics, cost-

effectiveness and high theoretical C_s [26]. The suitability of SnO_2 in composites has been demonstrated. For example, the SnO_2–MoS_2 microsphere composite electrode in a 3 M KOH electrolyte improved the C_s by 162% and 178% compared to MoS_2 and SnO_2, respectively [19]. In another study, a *2D* ZnO–SnO_2 electrode on an Au-modified SiO_2–Si wafer in 1 M KOH exhibited good reversibility, pseudo-capacitive characteristics, 86% Coulombic efficiency, and 96% C_s retention after 5000 cycles [4]. In addition, electrodes with a *flower-like* SnS_2–SnO_2 binary composite in KOH electrolyte showed battery-type electrochemical behaviour, rate capability of 73% and advanced C_s by 124% than the electrode of SnS_2 [27]. An electrode fabricated from MoS_2–SnO_2 binary nanocomposite attained a C_s advancement of 164% and 117% relative to that from MoS_2 and SnO_2, respectively [26]. Improvements were attributed to improved crystallinity in the nanocomposite. Similarly, *3D* graphene-TiO_2-SnO_2 ternary nanocomposite electrode in 6, 3 and 1 M KOH electrolyte also exhibited *battery-type* characteristics [28]. The champion and lowest performances were in the highest and lowest electrolyte concentration. The *3D* graphene-TiO_2-SnO_2 ternary nanocomposite in their study was ≈700% better than the binary TiO_2–SnO_2. A binder-free Sn–SnO_2-graphene quantum dots ternary nanocomposite was applied as an electrode of supercapacitors in 1 M KOH electrolyte and recorded ≈89% rate capability at 20 A g^{-1} [29]. Similarly, their Sn–SnO_2-graphene quantum dot-based electrode was 180% higher than that of Sn–SnO_2 binary nanocomposite. This is an illustration of the positive attributes of composite synthesis that result in morphological transformation. To sum up, a review of recent studies has shown a larger proportion of SnO_2 composites with other TMOs. Additionally, the SnO_2 positive modification in the energy storage of carbonaceous materials has been illustrated recently.

However, notable setbacks of SnO_2 include poor capacity retention attributed to low conductivity and large volume expansion during charge/discharge cycles. One underexplored way of overcoming the shortfalls of SnO_2 nanoparticles in supercapacitors is hybridisation with nitrogen-based carbonaceous materials, thus allowing a better electron pathway. Theoretically, carbonaceous nanomaterials as constituents in electrode materials for supercapacitors enhance the conductivity as well as mechanical stability of the material, thus significantly reducing the coherent volume expansion during charge/discharge cycles [4].

The reviewed works outline how both TMOs and g-C_3N_4 can potentially be enhanced through the synergism of physicochemical properties. In this study, inspired by the presented context, SnO_2 nanoparticles and WO_3 nanorods (NRs) were compared and employed to modify the electrochemical properties as well as the physicochemical characteristics of the carbonaceous component, g-C_3N_4. The physicochemical and electrochemical attributes of the fabricated electrodes from the as-synthesised g-C_3N_4 were compared with those of WO_3-g-C_3N_4 and SnO_2-g-C_3N_4 binary nanocomposites, and SnO_2-WO_3-g-C_3N_4 ternary nanocomposites were examined using various analytical techniques. To the best of our knowledge, the current work is the first report on SnO_2-WO_3-g-C_3N_4 ternary nanocomposites that were synthesised following a two-step hydrothermal procedure initially involving the synthesis of WO_3-g-C_3N_4, then repeated after the addition of SnO_2 precursor. The impact of the synthesis methods of electrode materials for supercapacitors has been realised as a significant factor [30]. Hence, the unique contributions of the binary and ternary nanocomposites underscore the potential of this approach in favourably transforming morphologies to create improved electro-active surfaces, enhance charge/discharge cycle stability, and increase thermal stability, among others. Furthermore, the application of WO_3 binary nanocomposites is commonly reported in acidic electrolytes. For more insights on performance, the current study of WO_3-based electrodes was carried out in basic electrolytes. Exploring hybrid electrochemical capacitor electrodes composed of SnO_2 modified with nitrogen-containing carbonaceous materials, such as g-C_3N_4, is a strategic step in addressing the limitations of SnO_2 nanoparticles for energy storage, as investigated in this work.

2. Materials and methods

2.1. Materials and reagents

All the reagents were used without further modification and processing. Analytical grade KCl (≥99%), polyvinylidene fluoride (PVDF), KOH (≥85%), $SnCl_2.2H_2O$, (98–103%) and HCl (32%) were purchased from Sigma Aldrich. $Na_2WO_4.2H_2O$, (95 %), 1-methyl-2-pyrrolidinone (NMP, ≥99%) and Melamine ($C_3H_6N_6$, 99%) were purchased from Alfa Aesar. $KMnO_4$ (99%) and NaCl were purchased from UNINAR and VWR Chemicals, respectively.

2.2. Preparation of graphitic carbon nitride and nanocomposites

2.2.1. The g-C_3N_4 nanosheets

The synthesis method for g-C_3N_4 was adapted from Praus et al. [31] In brief, 5 g of $C_3H_6N_6$ in a ceramic crucible was heated at 20 °C min^{-1} up to 450 °C and held for 2 h in a muffle furnace. The crucible was then cooled naturally to room temperature, and the obtained yellow material was crushed to obtain *3D* g-C_3N_4 powder, which was subsequently converted to *2D* g-C_3N_4 following a method by Li et al. [32] In this procedure, 0.2 g of *3D* g-C_3N_4 was dispersed in 200 mL deionised water and ultrasonicated at ambient temperatures and high frequency for 8 h. The products of this final step were then collected by centrifugation at 6000 rpm for 10 min up to 5 times. The collected product was then dried overnight at 60 °C in an air oven to obtain the *2D* g-C_3N_4 powder.

2.2.2. SnO_2-g-C_3N_4 nanocomposite

The SnO_2-g-C_3N_4 binary nanocomposite was synthesised by adding 0.1 g of the *3D* g-C_3N_4 to a solution of 0.1 g of $SnCl_2.2H_2O$ and 34 mL of 0.65 M HCl. The mixture was then stirred for 10 min at room temperature. The mixture was then transferred into a Teflon-lined stainless-steel autoclave and hydrothermally treated at 180 °C for 24 h in a hot air oven. Next, the autoclave was left to cool down to room temperature. The collected samples were then washed with deionised water and 98% ethanol (1:1) followed by centrifuging at 5000 rpm for 10 min each time up to 5 times. The products were dried at 60 °C in a hot air oven and subsequently annealed at 450 °C for 2 h to obtain the SnO_2-g-C_3N_4 binary nanocomposite.

2.2.3. WO_3-g-C_3N_4 nanocomposite

For the synthesis of WO_3-g-C_3N_4 binary nanocomposite, *3D* g-C_3N_4 was dispersed in 80 mL of 0.1 M $NaWO_4.2H_2O$ solution and ultrasonicated at ambient temperatures for 0.5 h at high frequency. Then, 0.45 g of NaCl was added to the dispersed solution and stirred for 1 h. The pH value of the resultant suspension was then adjusted to 2 using 3 M HCl solution. The solution was then transferred into a Teflon-lined stainless-steel autoclave. The autoclave was thereafter heated in a hot air oven at 180 °C for 20 h. The reactor was then cooled naturally to room temperature, and the samples were then collected, washed with deionised water and 98% ethanol (1:1) for 5 times. The collected product was then dried at 60 °C overnight to obtain the WO_3-g-C_3N_4 binary nanocomposite. The method was adapted from a procedure reported by Sandil et al. [33].

2.2.4. SnO_2-WO_3-g-C_3N_4 nanocomposite

To obtain SnO_2-WO_3-g-C_3N_4, 0.1 g of WO_3-g-C_3N_4 material was added to a solution of 0.1 g of $SnCl_2.2H_2O$ and 34 mL of diluted HCl (0.65 M). The mixture was then stirred at room temperature for 10 min and transferred into a Teflon-lined stainless-steel autoclave and hydrothermally treated at 180 °C for 20 h in a hot air oven. Consequently, the reactor was left to cool down to room temperature. The samples were then collected by washing with deionised water and 98% ethanol (1:1) at centrifugal speeds of 5000 rpm up to 5 times. The product was then dried at 60 °C in a hot air oven and annealed at 450 °C for 2 h to obtain the SnO_2-WO_3-g-C_3N_4 ternary nanocomposite.

2.3. Physicochemical characterisations

The physicochemical characterisation of the nanocomposites was determined using various techniques. The carbon, hydrogen and nitrogen contents of the g-C_3N_4 nanosheets were determined using a Thermofisher Scientific Flash 2000 analyser with a mass range of 140–150 mg. The surface morphologies and dimensions were studied using a JEOL JEM-2010 high-resolution electron transmission microscope (HR-TEM) with an accelerated voltage of 200 kV. The nanocomposite was prepared by dispersing it in ethanol and drop-coating it onto carbon-coated copper grids. X-ray photoelectron spectroscopy (XPS) was performed using an XSAM800 (Kratos, Manchester, UK) energy spectrometer operated for ≈80 s using Al Kα (1487 eV) radiation for excitation in constant analyser energy mode with a resolution of 0.2 eV under vacuum and taking an average of 40 scans to determine surface chemical compositions and valence state of the ternary composite. The N_2 adsorption/desorption analysis was done using a Micrometrics Flow Prep 060 with analysis at −195 °C. To determine surface area and pore volumes of the nanocomposites, the Brunauer-Emmett-Teller (BET) method was used, while the pore size distribution was determined using the Barret-Joyner-Halenda (BJH) measurements. The chemical moieties were elucidated by mixing nanocomposites with KBr to make pellets and then analysed through a Fourier Transform Infrared (FT-IR) method using a Bruker Tensor 27 FT-IR spectrometer in the 400-4000 cm^{-1} range. The phase and composition of the materials were investigated using powdered X-ray diffraction (XRD) recorded on a Bruker D2 Phaser diffractometer with Cu kα irradiation (30 kV) within 2θ range of 5–90°. Thermal stability of the nanocomposites was investigated using thermogravimetric analysis (TGA) using a Hitachi STA7200RV thermal analyser with a heating rate of 20 °C min^{-1} from 35 to 900 °C under an air atmosphere.

2.4. Electrochemical measurements

Ni foam (1 cm^2) was cleansed by ultrasonication in 3 M HCl for 0.5 h to remove the NiO layer and rinsed with deionised water and absolute ethanol, followed by drying at 70 °C for 12 h. After drying, a paste containing 80% of the nanocomposite active material, 10% carbon black, 10% PVDF and NMP was prepared and carefully smeared on the Ni foam current collector to fabricate the working electrodes. The working electrode loading was 100 mg cm^{-2}. The working electrodes were dried at 80 °C for 6 h before testing. The Ag/AgCl RE-1B reference electrode from ALS and the platinum electrode were used as the reference and the counter electrode, respectively. The electrolyte was 2 M KOH prepared using deionised water and analytical grade KOH salt.

The Gamry interface 1000E Electrochemical Workstation with a three-electrode configuration was utilised for electrochemical testing. Cyclic voltammetry (CV) and galvanostatic charge/discharge (GCD) studies were performed within −0.5 and 0.8 V potential range at required scan rates (50–500 mV s^{-1}). The GCD curves were evaluated at a current density of 0.01 A g^{-1} for 2000 cycles. The electrochemical impedance spectroscopy (EIS) experiments were conducted under an open circuit potential with a frequency between 0.1 and 100 kHz with a direct current voltage of 0.5 V.

3. Results and discussions

The section is in three parts, namely, qualitative analysis of pyrolysis product, physicochemical characterisation of nanocomposites and their study as electrode materials. To begin with, the transformation of *3D* g-C_3N_4 to *2D* g-C_3N_4 was signalled by a noticeable colour change from yellowish to white during ultrasonication. Following this observation, the first step was to establish if the synthesis of g-C_3N_4 was achieved using compositional analysis with a CHNS analyser. The percentage composition of the product prepared by pyrolysis of melamine was 32.25, 58.1 and 3.14% for C, N and H, respectively. Therefore, the product had a C: N ratio of ≈0.6, which was within range with other reports and comparable with the theoretical value of 0.75 for g-C_3N_4 [12,31,34]. Therefore, the product of pyrolysis was then referred to as g-C_3N_4.

3.1. Physicochemical characterization

This section discusses how the nanocomposite synthesis was used to tailor g-C_3N_4 properties.

3.1.1. Morphological, dimensional and surface species studies

The g-C_3N_4 was sheet-like, while SnO_2 was distorted spherical particulate in morphology and was both in the nanoscale range (Fig. 1a–b). The synthesised WO_3 was rod-like in morphology with diameters as low as 5 nm, hence, it is thereafter referred to as nanorods (NRs) (red arrow in Fig. 1c). Furthermore, the in-situ hydrothermal synthesis of WO_3 NRs on g-C_3N_4 sheets to form a composite yielded WO_3 NRs with an average length of ≤200 nm and a diameter ≤10 nm, thus, qualify to be named a nanocomposite (Fig. 1d). The nanocomposite comprises nanosheets with mostly distinct edges (red arrow in Fig. 1d), however, some g-C_3N_4 curled up to form tiny nanosheets, particularly when in a nanocomposite with SnO_2 (Fig. 1e). The subsequent hydrothermal treatment of g-C_3N_4 materials thermodynamically favours the rotation of the N–N bonding of the intrinsic vacancies between tri-s-triazine and triazine moieties in g-C_3N_4, hence, hinders the growth of larger-sized layers [35]. In addition, the contrast in the sizes of the nanosheets can be attributed to the uneven temperature distribution during condensation because the current method did not involve stirring. Unlike most materials in the graphene family, the studied g-C_3N_4 revealed slight buckling attributed to the repulsion effect of the lone pairs from the nitrogen atoms coordinated within the triazine rings. Furthermore, the edges of the nanosheets depict mono-layered g-C_3N_4 nanostructures with patches of stacked sheets and smooth surfaces in the WO_3-g-C_3N_4 nanocomposite (Fig. 1d) [36]. The dark spots represent sites of stacked layers with the transparent layers, indicative of the increase in interlayer separation (Fig. 1d). Interestingly, the nanocomposite morphology with g-C_3N_4 nanosheets and SnO_2 nanoparticles changes from planar sheet-like to planar rod-like structures with an average diameter of ≤10 nm with distinct edges and smooth surfaces (green arrows Fig. 1e). This was due to the effect of pressure and temperature of the hydrothermal treatment step [37]. The SnO_2 nanoparticles nucleate within the triazine units, causing a size reduction of the g-C_3N_4. Moreover, the high-resolution micrographs display lattice fringes (red circles in Fig. 1e) of the highly crystalline SnO_2 nanoparticles with an average diameter of ≈8 nm.

The discrete edges of layered g-C_3N_4 with asymmetrical sheets were retained in SnO_2-WO_3-g-C_3N_4 nanocomposite (red circles in Fig. 2a). The relatively small sheet sizes of g-C_3N_4 are ascribed to the presence of the Sn precursor during nucleation of SnO_2 nanoparticles in in-situ hydrothermal synthesis, which is evident on the SnO_2-g-C_3N_4 (Fig. 1e) and absent in WO_3-g-C_3N_4 (Fig. 1d) nanocomposite. In addition, the small g-C_3N_4 sheet sizes can be attributed to the rotation of intrinsic vacancies between triazine and tri-s-triazine, promoted by hydrothermal treatment. The SnO_2 nanoparticles with an average diameter of 2 nm were well distributed within the WO_3-g-C_3N_4 matrix in the SnO_2-WO_3-g-C_3N_4 nanocomposite (red circles in Fig. 2b). The uniform growth of SnO_2 nanoparticles on WO_3 NRs surfaces is suitable for enhancing ion diffusion for better energy storage capabilities [38]. In addition, the crystallinity of WO_3 NRs with visible lattice fringes was clear in the SnO_2-WO_3-g-C_3N_4 nanocomposites (Fig. 2c–d).

Qualitatively, the elements present in the SnO_2-WO_3-g-C_3N_4 ternary nanocomposite were C, N, O, Sn and W (Fig. 2e). The binding states of components of g-C_3N_4 located at 284.6, 399.7 and 401.8 eV were ascribed to graphitic sp^2-hybridized carbon in the framework (C1s), pyridinic-like nitrogen within the C–N═C of the triazine ring (N1s) and tertiary/graphitic nitrogen atoms incorporated into the graphene-like sheets (N–$(C)_3$), respectively (Table 1, Fig. 2e, and Fig. S2 in the

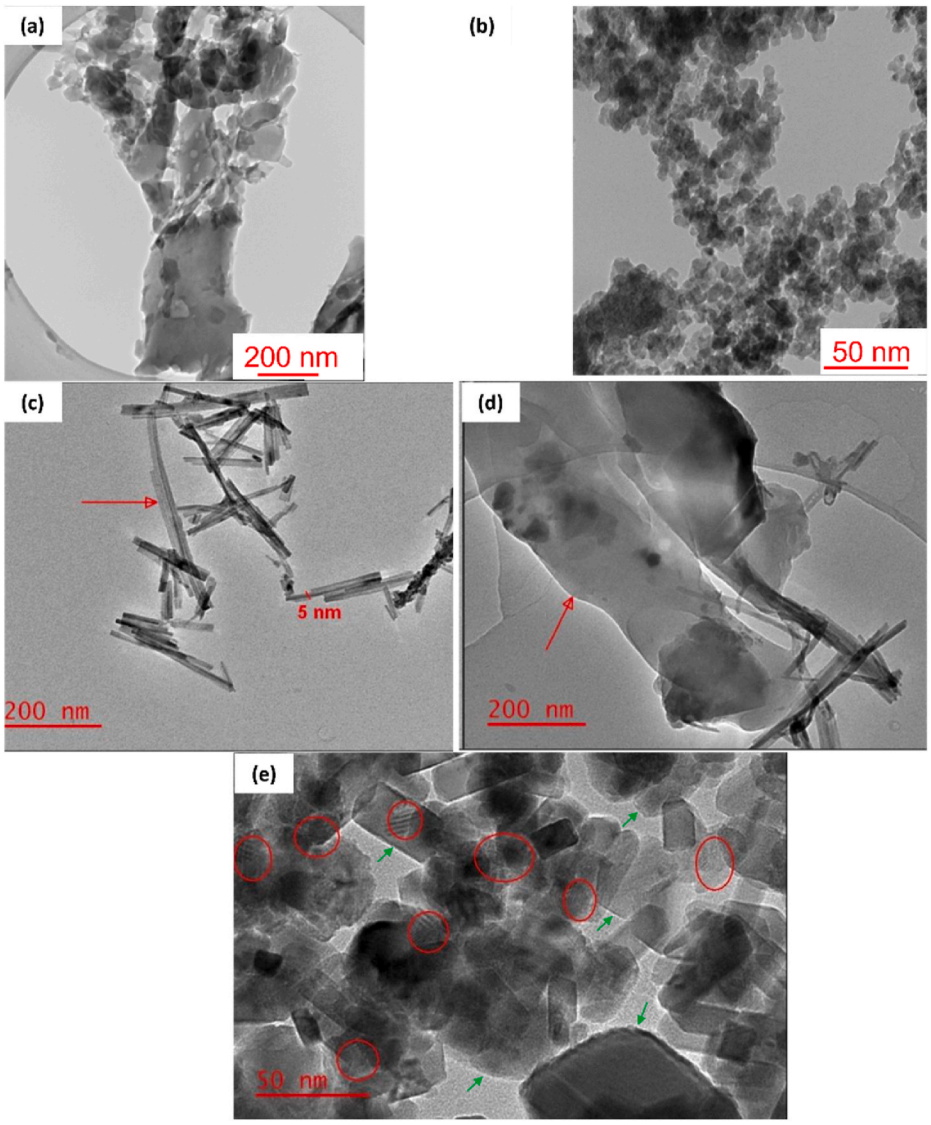

Fig. 1. The TEM micrographs of (a) g-C_3N_4, (b) SnO_2 NPs, (c) WO_3 nanorods, (d) WO_3-g-C_3N_4, and (e) SnO_2-g-C_3N_4.

Online Resource File) [39]. Interestingly, the atomic composition of pyridinic and graphitic nitrogen in the nanocomposites was approximately equal. The pyridinic N moieties have been reported to induce pseudocapacitance in carbonaceous materials, while graphitic N enhances conductivity [2,40]. Like other reports, the presence of O1s within 531–532.9 eV is associated with residual oxygen from synthesis reagents and adsorbed water (Table 1 and Fig. 2e). However, the majority of the O1s (peak at 530.5 eV) in the ternary nanocomposites originated from TMOs, indicating that compositing raised surface oxides (Table 1). The C1s peak was deconvoluted into three peaks, with the C–C and C–C═C peaks assigned to typical adventitious and sp^2 carbons in g-C_3N_4 from the pyrolysis process [32,41]. The peaks at 286.1 eV, along with those at 531.7 and 532.9 eV, were assigned to C–O and C═O groups (Table 1 and Fig. 2e). The peaks at 487.0 and 35.4 eV suggest the possible presence of both SnO and SnO_2 in the ternary composite, while only WO_3 was present. The higher atomic concentration at the surface was attributed to morphology differences between WO_3 NRs and SnO_2/SnO nanoparticles (Table 1). The smaller SnO nanoparticles can feasibly penetrate the layers of g-C_3N_4. This is expected to influence the electrochemical processes of the electrode, where the impact of WO_3 will be more on the surface.

3.1.2. Textural analysis

Notably, the surface area of the nanocomposite drastically decreased to 23% that of g-C_3N_4 in the WO_3-g-C_3N_4 binary nanocomposite (Table 2). This was rationalised by employing TEM micrographs, which indicated that subsequent hydrothermal synthesis of the binary nanocomposite induced slight agglomeration of individual g-C_3N_4 sheets with a decrease in planar size (Fig. 1d). This could have decreased the accessibility of pores during N_2 adsorption/desorption experiments. Relative to pristine g-C_3N_4, the SnO_2-g-C_3N_4 binary nanocomposite achieved a 160% surface area, while the SnO_2-WO_3-g-C_3N_4 ternary nanocomposite was 133%. This trait cannot be attributed to a decline/gain in pore volume effect because of the negligible deviations from g-C_3N_4 when compared to the surface area changes, which could be within error margins. A possible reason is the synergy decline brought by WO_3 NRs in the ternary nanocomposites, while the SnO_2 nanoparticles induced positive synergistic effects, conceivably through the observed morphological transformations (Figs. 1 and 2 and Table 2). Additionally, the decrease in size of g-C_3N_4 in the SnO_2-g-C_3N_4 and the uniform distribution of SnO_2 nanoparticles within the nanocomposite matrix is a feasible explanation for the highest surface area recorded, while the NR morphology of WO_3 was the main reason for the lower value (Fig. 2c–d and Table 2). The other possible rationale is the involvement of

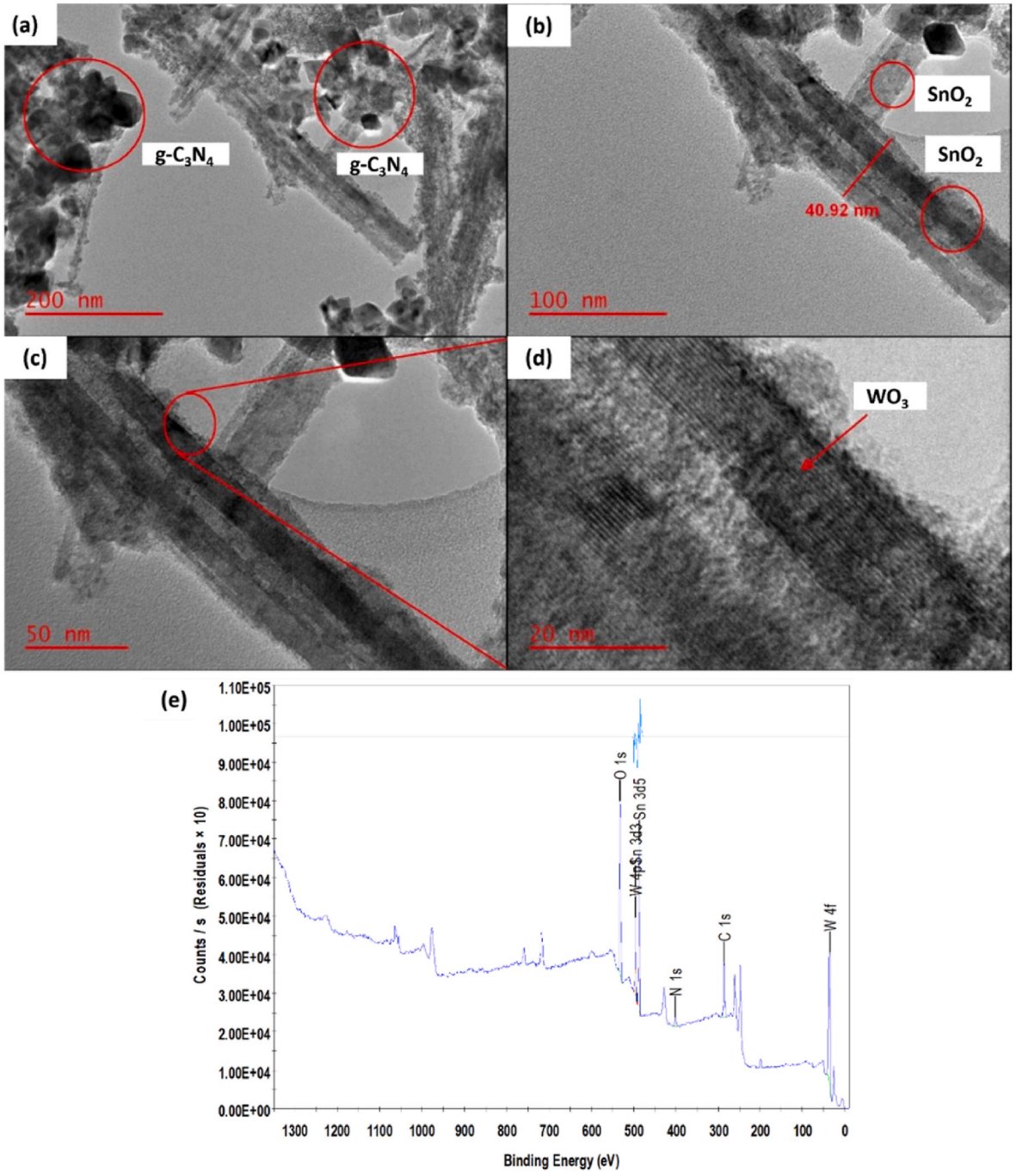

Fig. 2. The TEM micrographs of SnO_2-WO_3-g-C_3N_4 at (a) 200, (b) 100, (c) 50 and (d) 20 nm to illustrate different nano-structural features, and (e) the survey spectrum from XPS.

Table 1
The elemental analysis using X-ray photoelectron spectroscopy.

Deconvoluted peak	Binding energy (eV)	FWHM (eV)	Atomic %
W4f (WO_3)	35.4	1.2	9.14
C1s (C–C)	284.6	1.3	26.84
C1s (C–O)	286.1	1.3	6.15
C1s (C═O)	288.5	1.3	3.59
N1s (pyridinic)	399.7	2.4	2.55
N1s (graphitic)	401.8	2.4	2.52
Sn3d (SnO; SnO_2)	487.0	1.3	4.77
O1s (TMOs)	530.5	1.4	32.68
O1s (C–O)	531.7	1.4	7.73
O1s (C═O)	532.9	1.4	4.03

Table 2
Textural properties from the nitrogen sorption/desorption analysis.

Material	Surface area (m^2 g^{-1})	Average diameter (nm)	Pore volume (cm^3 g^{-1})
g-C3N4	22	24.0	0.1
WO_3-g-C3N4	5	33.8	0.0
SnO_2-g-C3N4	35	16.6	0.1
SnO_2-WO_3-g-C3N4	24	15.4	0.1

ultrasonic treatment and more intense stirring in WO_3-g-C_3N_4 and SnO_2-g-C_3N_4, respectively, before loading into the autoclave. The stirring possibly induced more detangling outcomes.

3.1.3. Functional group analysis

The chemical interactions in the nanocomposites were studied through FTIR analysis (Fig. 3a–d). The sharp peak at ≈800 cm^{-1} is attributed to the breathing mode of tri-s-triazine ring modes [1,15]. The broad peak between 2900 and 3600 cm^{-1} is rationally the free uncondensed terminal primary or secondary amino groups (-NH_2 or = NH), with the absorption bands between (1200-1600 cm^{-1}) owing to the heterocyclic C=N (i.e., C–NH–C bridges and (N-$(C)_3$) of the g-C_3N_4 network (Fig. 3a–d) [1,12]. The absorption band at ≈3200 cm^{-1} can also be ascribed to the O–H stretching of physiosorbed water molecules, thus agreeing with XPS deductions. Logically, the presence of physiosorbed water molecules in g-C_3N_4 is feasibly facilitated by H-bonding of water molecules to the surface due to the presence of amino groups (Fig. 3a). In brief, the successful g-C_3N_4 synthesis was correlated with the identified chemical structure units.

The characteristic peaks of both WO_3 and g-C_3N_4 were observed in the spectrum of the WO_3-g-C_3N_4 nanocomposite (Fig. 3b). The broad band 615-800 cm^{-1} was also characteristic of the O–W–O peak that could have overlapped with the aromatic peaks of heterocyclic C–N bands. The red shift of the primary and secondary amine stretching, from ≈3200 cm^{-1}, in binary WO_3-g-C_3N_4 nanocomposite was suggestive of the formation of the chemically-linked composite (Fig. 3b). For the SnO_2-g-C_3N_4 binary nanocomposite, an overlap of the 600-900 cm^{-1} vibrational modes was possible (Fig. 3c). The SnO_2-WO_3-g-C_3N_4 ternary composite showed characteristic peaks of the g-C_3N_4, SnO_2 and WO_3 individual components (Fig. 3d).

3.1.4. Crystallinity studies

XRD diffractogram revealed two distinct peaks at 2θ ≈ 14° and 27.3°, which were assigned to (100) tri-s-triazine units with hydrogen bond connections and (002) for stacked lattice planes of the conjugated hexagonal aromatic rings of g-C_3N_4 with weak van der Waals interlinkages (Fig. 4a, JCPDS 87–1526) [42]. Therefore, the pattern can be ascribed to an orthorhombic arrangement with lattice constants a ≈0.73, b ≈0.85, and c ≈65 nm [12]. The (100) and (002) g-C_3N_4 peaks were visible in the WO_3-g-C_3N_4 binary nanocomposite (Fig. 4b). Additionally, the diffraction patterns of WO_3 in WO_3-g-C_3N_4 were all indexed for the hexagonal phase (ICSD card number 80634, Fig. 4b). The hexagonal phase of WO_3 is the most ideal for supercapacitor applications [43]. At 2θ ≈ 26.5°, the peak broadening was indicative of the overlapping (002) plane of g-C_3N_4 and the (200) plane of hexagonal WO_3. Therefore, the WO_3-g-C_3N_4 binary nanocomposite contained both components.

In addition to the obscured g-C_3N_4 XRD peaks, at 2θ ≈ 42°, 44°, 50°, 54°, 59°, 77°, 83°, 86° and 93° peaks were indexed to (100), (101), (102), (004), (103), (110), (112), (006) and (201) SnO_2 planes in SnO_2-g-C_3N_4, respectively (Fig. 4c). The sharp diffraction peaks suggest the existence of higher crystallinity of SnO_2, which resulted in the obscuring of g-C_3N_4 after hydrothermal reaction. The diffractograms of the ternary

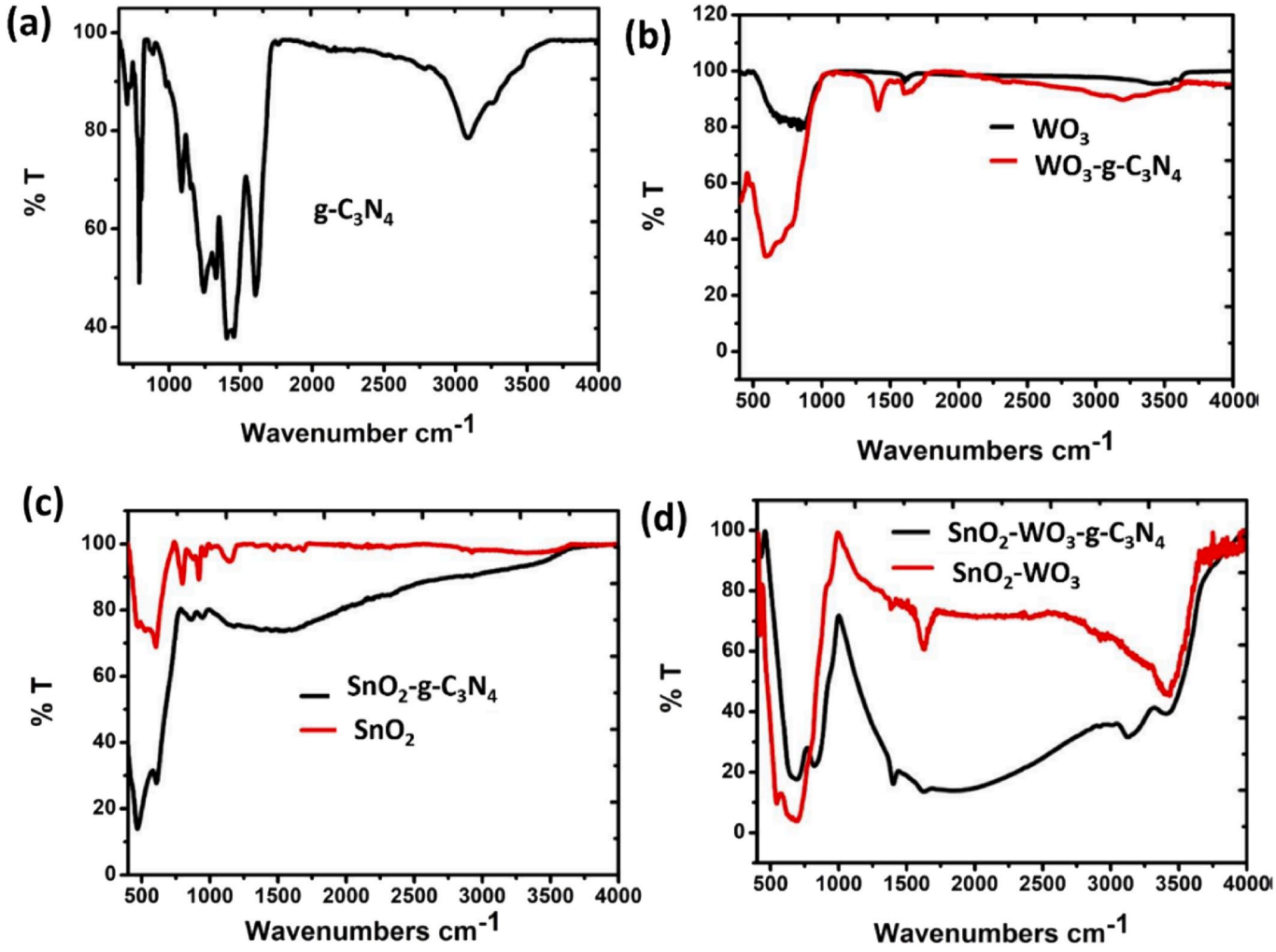

Fig. 3. The functional moieties in (a) g-C_3N_4, (b) WO_3-g-C_3N_4, (c) SnO_2-g-C_3N_4 and (d) SnO_2-WO_3 and SnO_2-WO_3-g-C_3N_4.

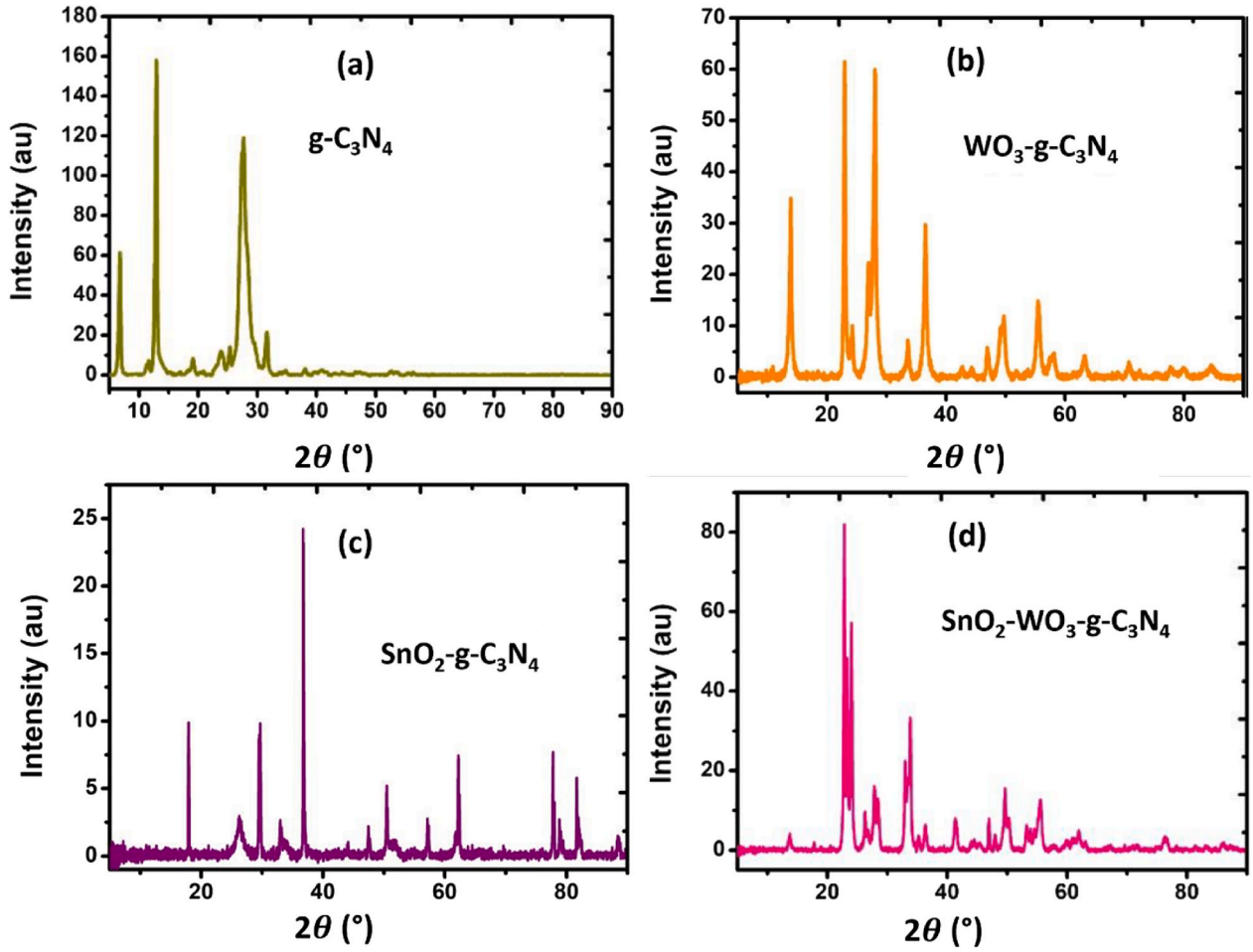

Fig. 4. The XRD diffractograms for (a) g-C_3N_4, (b) WO_3-g-C_3N_4 (c) SnO_2-g-C_3N_4 and (d) SnO_2-WO_3-g-C_3N_4.

composites exhibited the characteristic peaks of the WO_3 and SnO_2 complexed in pristine g-C_3N_4 through a subsequent in-situ hydrothermal reaction (Fig. 4d). Similarly, the diffractograms of the SnO_2-WO_3-g-C_3N_4 ternary nanocomposite did not present distinct graphitic peaks for g-C_3N_4 owing to the overlapping peaks and the stronger signal of the TMOs (SnO_2-WO_3) detectable within the range. Comparatively, from peak sharpness, SnO_2-WO_3-g-C_3N_4 was more and less crystalline than WO_3-g-C_3N_4 and SnO_2-g-C_3N_4 (Fig. 4b–d), respectively.

Crystallinity using Raman spectroscopy displayed characteristic breathing modes of the triazine ring, disordered D-band and the graphitic G-band of g-C_3N_4 at 707, 1230 and 1600 cm^{-1} (Fig. 5a) [12,13,31]. The resolution of g-C_3N_4 peaks between 1000 and 1500 cm^{-1} is relatively low due to the weak intensities of the peaks induced by liquid stripping during ultrasonication. Moreover, the representative Raman

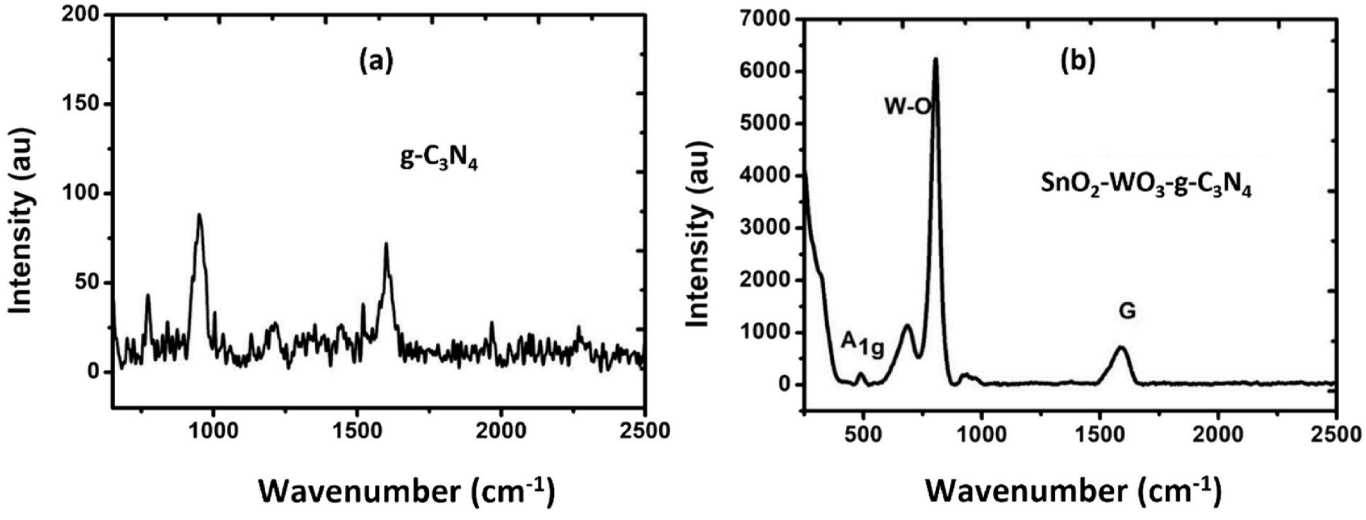

Fig. 5. Representative Raman spectra for (a) g-C_3N_4 and (b) SnO_2-WO_3-g-C_3N_4.

spectra of the SnO_2-WO_3-g-C_3N_4 nanocomposite showed characteristic peaks of g-C_3N_4 and WO_3 NRs at 1600 cm^{-1}, and between 710 and 812 cm^{-1} assigned to the O–W–O and W–OH_2 stretching modes of WO_3 (Fig. 5b) [19,22]. This could have been influenced by the physiosorbed water molecules. The apparent peak at 949 cm^{-1} is due to the symmetrical vibrational mode of the W═O terminal of the clustered boundaries of individual WO_3 NRs [22]. The peaks at 806 cm^{-1} are the O–W–O stretching vibration typical of bridging oxygen molecules of WO_3 [19,22]. The A_{1g} peak at 500 cm^{-1} was due to SnO_2 nanoparticles (Fig. 5b). The absence of most typical SnO_2 peaks was viably due to the overlapping of g-C_3N_4 and SnO_2 peaks due to the contrast in crystallinity between the two. The D-band disappeared due to enhanced crystallinity in the nanocomposites and may suggest that the TMO were deposited on the defects [44]. Similar traits were observed in the binary nanocomposites.

3.1.5. Thermogravimetric analysis

The slight dip in weight% between 100 and 150 °C for g-C_3N_4 was due to moisture loss from the H-bonded water (Table 1, Figs. 3a and 6). The drastic weight loss between 500 and 700 °C was a signal of the decomposition of the graphite sp^2 framework carbons in the tri-s-triazine units. From the analysis, it is evident that pristine g-C_3N_4 was thermally stable until 600 °C and fully decomposed at ≈700 °C owing to thermal decomposition to NH_3, C_2N_2 and CHN moieties (Fig. 6) [12,13]. The WO_3 lowered thermal stability of the WO_3-g-C_3N_4 binary nanocomposite with a weight loss of ≈45 wt% at ≈400 °C (Fig. 6). The thermograms illustrate that SnO_2 within the g-C_3N_4 framework improves the thermal stability significantly beyond 800 °C though with minimal weight loss (≈3%) at low temperatures (<450 °C) due to physiosorbed water molecules of the binary nanocomposite (Fig. 6). The SnO_2-WO_3-g-C_3N_4 ternary nanocomposite also showed higher thermal stability, even at temperatures >900 °C, while only <1% wt.% loss occurred at low temperatures (≈60 °C). This also indicates a decline of physiosorbed water molecules and the synergistically stronger interactions in SnO_2-WO_3-g-C_3N_4 matrix. This feasibly reflects a pronounced chemical interaction between the TMOs nanostructures with g-C_3N_4 nanosheet, leaving few amino moieties for H-bonding with water.

3.2. Electrochemical measurements

Three techniques, namely, CV, EIS and GCD, were used to ascertain the improvements in the nanocomposites as electrodes relative to g-C_3N_4.

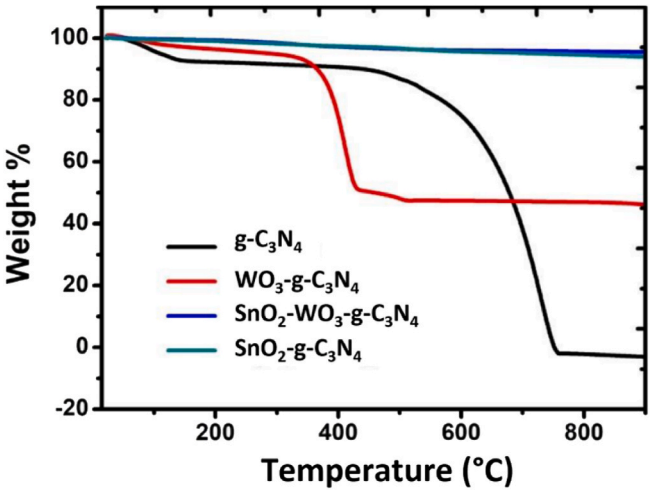

Fig. 6. Thermal analysis of g-C_3N_4 and the studied nanocomposites in air.

3.2.1. Study of electrode enhancements through the cyclic voltammetry technique

The voltammograms of the electrodes fabricated from as-synthesised g-C_3N_4 exhibited pseudo EDLC behaviour; therefore, as-synthesised g-C_3N_4 had noticeable reversibility (Fig. 7a). This is a characteristic phenomenon of most carbonaceous materials due to mostly contributions from outer surfaces [30]. Also, the current response rose as the scan rate was raised with a pronounced non-superimposition of voltammograms. This behaviour of the as-synthesised g-C_3N_4 has been highlighted as a manifestation of EDLC/quasi-reversible redox (diffusion-controlled) hybrid mechanism traits [30]. The voltammogram of the electrode made of WO_3-g-C_3N_4 nanocomposites exhibits a similar *leaf-like* quasi-rectangular shape, though with improved reversibility relative to that from g-C_3N_4 (Fig. 7b). Relative to electrodes from WO_3-g-C_3N_4, SnO_2-g-C_3N_4 binary nanocomposites had better symmetrically shaped voltammograms indicative of a more EDLC character with diffusion-controlled contributions (Fig. 7c). Similarly, to WO_3-g-C_3N_4, the voltammogram of electrodes from ternary SnO_2-WO_3-g-C_3N_4 nanocomposites displayed quasi-EDLC behaviour with a visible faradaic peak at +0.2 V, signalling pseudo-capacitance contributions (Fig. 7b and d), possibly a manifestation of the Faradaic nature of WO_3 NRs. In addition to the contributions of the pyridinic and graphitic N moieties of g-C_3N_4, pseudocapacitance can be accounted for through the equation:

$$WO_3 + xNa^+ + xe^- \rightarrow Na_xWO_3 \quad \text{(i)}$$

The integrated area of the voltammograms of the electrode fabricated from nanocomposites was greater than that of the as-synthesised g-C_3N_4 (Fig. 7a–d). Hence, from the CV technique, the ascending trend in C_s enhancement 50 mV s^{-1} from that of the electrodes of the as-synthesised g-C_3N_4 was SnO_2-g-C_3N_4 (119 %) < WO_3-g-C_3N_4 (177 %) < SnO_2-WO_3-g-C_3N_4 (192 %). This is a clear indication of better synergism in WO_3-g-C_3N_4 than in SnO_2-g-C_3N_4. A probable reason for this is the higher concentration of WO_3 on the surface, which therefore has more influence on the surface energy storage (Table 1).

Two known positive attributes of compositing TMOs with carbonaceous materials, which are most likely responsible for the observed improvements, are morphological and crystallinity enhancement achieved by the following hydrothermal protocol [16]. This is possible because energy storage processes that occur on both the electrode outer surface and in pores through diffusion-controlled processes are influenced by morphology and crystal structure. Moreover, the trend highlights that binary and ternary nanocomposites with WO_3 and SnO_2 improved the energy storage abilities of g-C_3N_4 through synergism from observed morphological transformations and ultimate electro-active surfaces. Similar traits have been viably attributed to increased electrical conductivity, electro-active surface area, suitability of pore structures for optimal ionic mobility between the electrode/electrolyte interface and electrochemical stability during testing [19,20].

3.2.2. Nanocomposite effect on g-C_3N_4 study via electrochemical impedance spectroscopy

The impact on ion transport attributes of g-C_3N_4 was studied through EIS (Fig. 8). For this technique, the equivalent circuit model used was the constant phase element (CPE) (Fig. 8a). For all the studied materials, there was no noticeable semi-circle in the high frequency region (Inserts in Fig. 8). This was attributed improved conductivity possibly brought by the graphitic N moieties in the framework of g-C_3N_4. The WO_3-g-C_3N_4 binary nanocomposite exhibits charge transfer (Rct) and solution resistances (Rs) of 0.48 Ω and 216 Ω, respectively. This was a significant lowering of Rct from that of g-C_3N_4 (Rct: 1.26 Ω). The SnO_2-g-C_3N_4 binary nanocomposites also suppressed the Rct of g-C_3N_4 from 1.26 to 0.8 Ω. Hence, Rct rationalised the superior energy storage capabilities, observed with the CV technique, of WO_3-g-C_3N_4 than SnO_2-g-C_3N_4. The lower Rct of the binary nanocomposites suggests more efficient electron mobility between the current collector/electrode/electrolyte interface

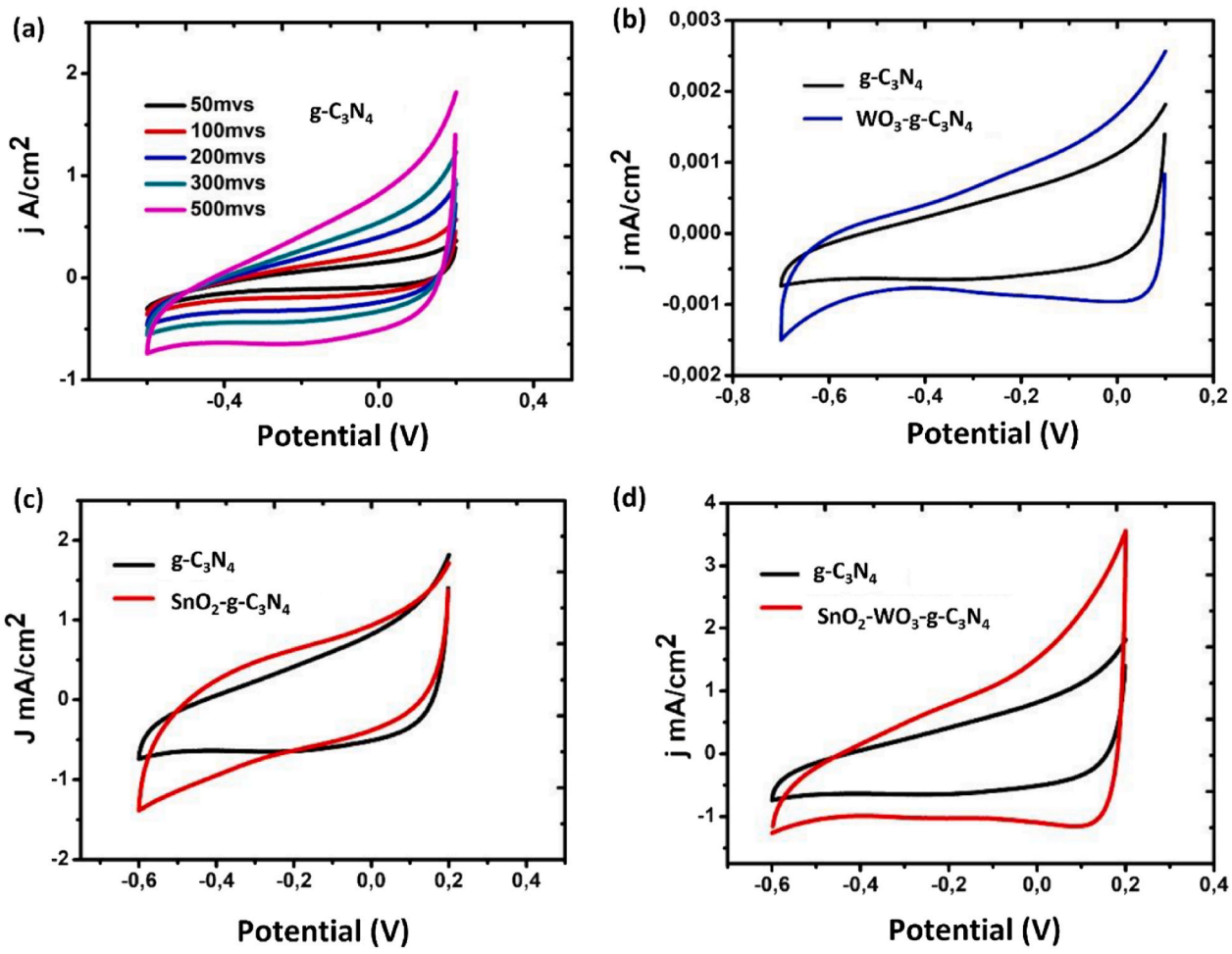

Fig. 7. The voltammograms at different scan rates for (a) g-C_3N_4, and at 500 mV s^{-1} for (b) WO_3-g-C_3N_4, (c) SnO_2-g-C_3N_4 and (d) SnO_2-WO_3-g-C_3N_4.

than in g-C_3N_4, owing to the Faradaic activity induction of WO_3 NRs and additional contributions of SnO_2 nanoparticles. This can also be an attribute of nano-morphological transformations in the nanocomposites (Fig. 2). However, from the fitted circuit model, the SnO_2-WO_3-g-C_3N_4 ternary nanocomposite resulted in a higher Rct value (1.55 Ω) than that of pristine g-C_3N_4. This suggests that there were other contributing factors to the enhanced energy storage in the ternary nanocomposites relative to the as-synthesised g-C_3N_4, such as the possible contribution of fast charge transport and facile intercalation of electrolyte ions owing to improved electro-active surface area and uniform morphology [19,38].

For supercapacitors, an ideal capacitive behaviour is characterised by a vertical line in the low-frequency region [21,23]. The Nyquist plot of an electrode of the WO_3-g-C_3N_4 binary nanocomposite exhibits an oblique curve, but steeper than that from the g-C_3N_4 (Fig. 8b), confirming a pseudocapacitive-based behaviour of the material and improved ion diffusion properties in the binary nanocomposite. This concurs with the CV technique, illustrating improved capacitance. Comparatively, the Nyquist plot of the SnO_2-g-C_3N_4 binary nanocomposite electrode demonstrates ion diffusion processes similar to pristine g-C_3N_4 (Fig. 8c). The EIS results (Fig. 8d) align with the CV measurements, indicating excellent capacitive behaviour of the SnO_2--WO_3-g-C_3N_4 ternary nanocomposite. Relatively, the more vertical line curve of the Nyquist plot suggests better ion diffusion processes than the pristine TMOs (WO_3 and SnO_2, Fig. 8d).

3.2.3. *Tailoring of g-C_3N_4 study by the galvanostatic charge/discharge measurements*

The influence on electro-capacitive behaviours of the as-synthesised g-C_3N_4 through a synthesis of nanocomposites was further evaluated through GCD experiments (Fig. 9a–f). Relatively, the GCD curves of WO_3-g-C_3N_4 binary nanocomposite were the most symmetrical inverted triangles, followed by the ternary nanocomposite (Fig. 9a–c). This demonstrates superior charge storage induced by the positive synergistic impact of WO_3 on Coulombic efficiency and electrochemical reversibility of the synthesised nanocomposites [3,14,20].

The non-symmetrical nature of the GCD curves of the current nanocomposites relative to the electrodes of the as-synthesised g-C_3N_4 at 200th cycle is illustrative of low Coulombic efficiency, poorer electrochemical reversibility, diffusion-controlled and redox capacitive characteristics of the electrode (Fig. 9d–f). The electrodes of g-C_3N_4 relative to WO_3-g-C_3N_4 binary nanocomposites displayed both faster charging and discharging times (Fig. 9d). For the electrode of SnO_2-g-C_3N_4 the charging times were comparable to g-C_3N_4 and this correlates with similar ion diffusion processes (Fig. 8c). Intriguingly, the binary nanocomposite achieved longer discharge times, thus, a positive indicator of improvement from energy storage capabilities of g-C_3N_4 (Fig. 9e). The non-symmetrical GCD curves of SnO_2-g-C_3N_4 suggest redox activities that facilitate pseudocapacitance conceivably through:

$$SnO_2 + H_2O + e^- \rightarrow SnOOH + OH^- \quad \text{(ii)}$$

$$SnOOH + e^- \rightarrow SnO + OH^- \quad \text{(iii)}$$

In addition, the SnO_2-WO_3-g-C_3N_4 ternary nanocomposite attained shorter charging and longer discharging times than the as-synthesised g-C_3N_4 (Fig. 9f). The longer discharge times of the ternary nanocomposites are a manifestation of additional Faradaic behaviour of the TMOs to the

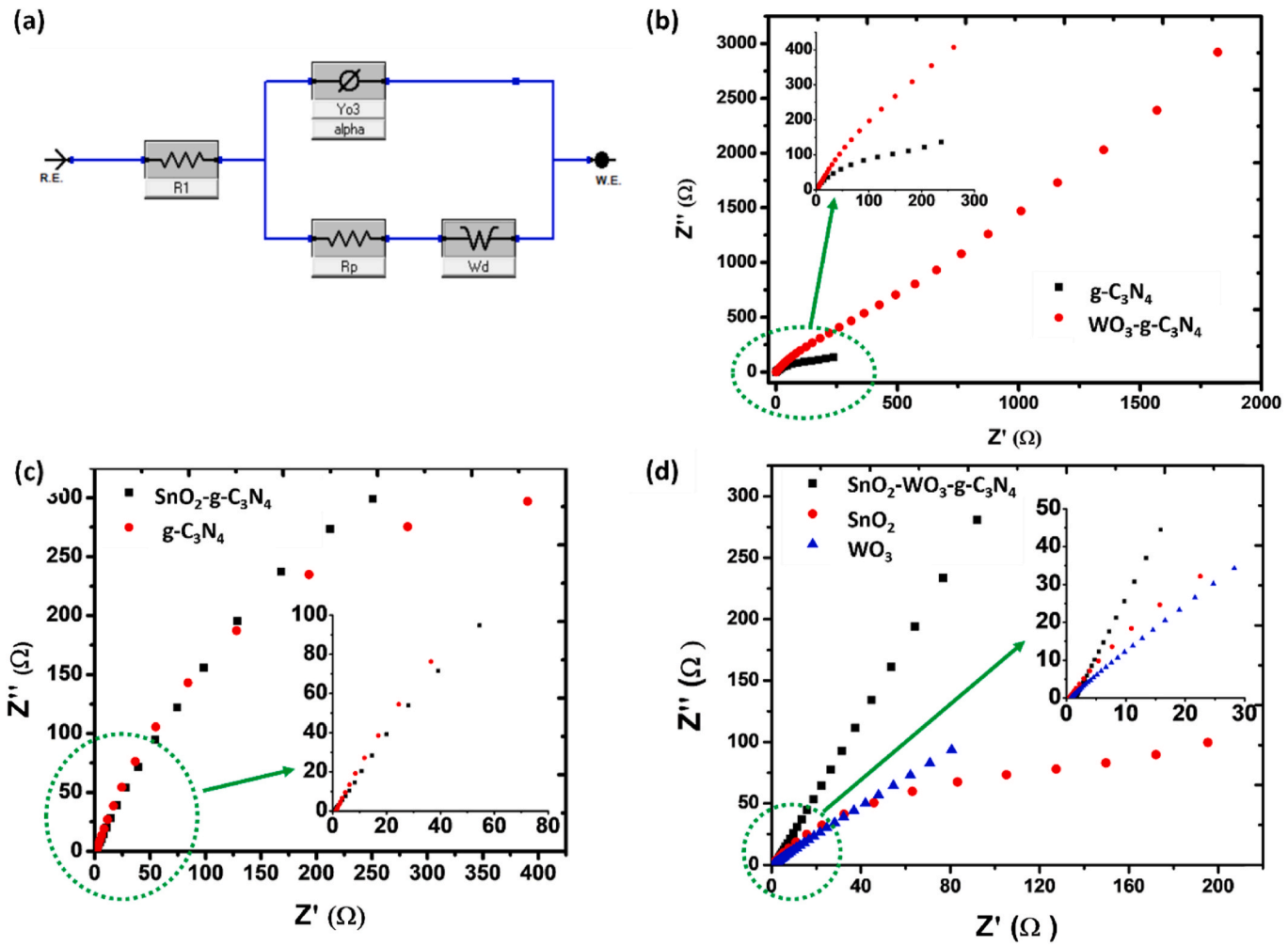

Fig. 8. (a) Representative CPE ESR circuit and EIS spectra comparison to g-C_3N_4 for (b) WO_3-g-C_3N_4, (c) SnO_2-g-C_3N_4 and (d) WO_3–SnO_2-g-C_3N_4 relative to individual TMOs.

N-rich moieties and of the g-C_3N_4 carbonaceous framework (Fig. 9d–f). In brief, the binary and ternary nanocomposites improved energy storage capabilities of g-C_3N_4, indicating a good synergistic relationship between components with enhanced ionic mobility between the electrolyte/electrode interface. Only the ternary nanocomposite dropped slightly in IR with an increase in cycle numbers (Fig. 9a–c). Relative to g-C_3N_4, only the WO_3-g-C_3N_4 binary nanocomposite had a negligible IR drop, and this is an indication of the champion performance in this regard (Fig. 9d–f).

3.2.4. *Investigating the cycle stability effect of nanocompositing g-C_3N_4*

The GCD curve of WO_3-g-C_3N_4 binary nanocomposite at the 200th cycle was comparable to the 2000th cycle with a slightly shorter discharge time of ≈5s (relative 7.5 s 200th cycle, respectively, Fig. 10a), signalling stability of Coulombic efficiency over this range. On the contrary, the electrode from the SnO_2-g-C_3N_4 binary nanocomposite had both longer charging period to maxim potential of ≈17 s (relative to 16 s) and discharge of ≈10 s (relative to ≈5 s) times after the 2000th cycle (Fig. 10b). The charging and discharge times were ≈55 and ≈35 s at the 2000th cycle compared to ≈30 s charge/discharge duration after the 200th cycle for the SnO_2-WO_3-g-C_3N_4 ternary nanocomposite (Fig. 10c). This could be an attribute of morphological stability in ternary nanocomposite (Fig. 6) that culminated on a need for longer time to achieve appreciable wettability over cycle numbers. This aligns with the phenomenon reported in lithium nickel manganese cobalt oxide batteries (NCM lithium-ion battery) [45].

The capacitance retention curve of the electrode fabricated from WO_3-g-C_3N_4 nanocomposite was characterised by an activation point at < 50 cycles and the optimum performance zone at > 200 cycles with an optimum cycle stability of ≈96 % of the initial C_s that was stable up to the studied 2000th cycle (Fig. 10d). This corroborated the GCD curve characteristics between the 200th and 2000th cycles (Fig. 10a) and is a testament to the superior stability of the electrode from the binary nanocomposite. The most probable reason is synergistic prevention of volume fluctuations in the WO_3-g-C_3N_4 binary nanocomposite-based electrode during charge/discharge cycles [38]. The capacity retention of the electrode from SnO_2-g-C_3N_4 binary nanocomposite was >80 % and >70 % after the 1000th and 2000th cycles, respectively (Fig. 10e). The diminishing capacitance >1000 cycles is attributed to the slight decrease of electro-active sites on the surface of the electrode. Also, the low capacitance in initial cycles is attributed to the electrochemical behaviour of the SnO_2, which requires a period of activation to wet the electrode completely through the circulation of electrolyte ions within the electrode active material.

The amplified electrochemical performance of the electrodes is attributed to the binary nanocomposite architecture with a higher BET surface area than that of pristine g-C_3N_4. Additionally, the pseudocapacitive nature of SnO_2-WO_3 nanostructures induces rapid electrolyte ion and electron mobility between the electrode/electrolyte interface. The cycle stability of the electrodes fabricated from the SnO_2-WO_3-g-C_3N_4 ternary nanocomposites was characterised by a drastic capacitance decay beyond the 800th cycles to 60 % from >100 % (Fig. 10f). This is a

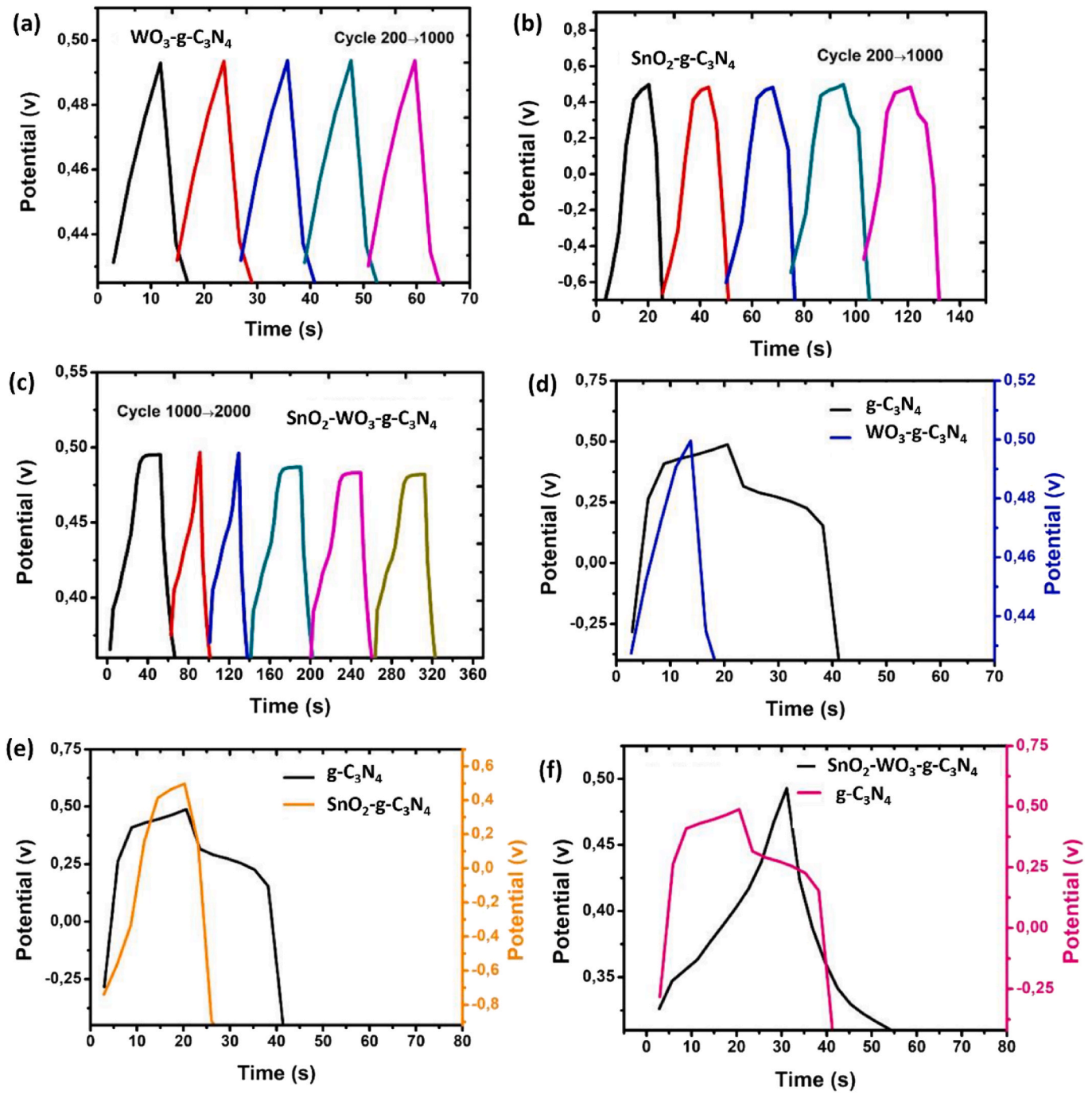

Fig. 9. The GCD curves of (a) WO_3-g-C_3N_4, (b) SnO_2-g-C_3N_4 and (c) SnO_2-WO_3-g-C_3N_4, and GCD curve at 200th cycle relative to g-C_3N_4 for (d) WO_3-g-C_3N_4, (e) SnO_2-g-C_3N_4 and (f) SnO_2-WO_3-g-C_3N_4.

significantly low lifespan at optimum performance. The poor cycle stability may be rationalised by immense internal stress and volume expansion, induced by ion movement during charge/discharge cycles, that causes electrode pulverisation [25,46]. In this context, the SnO_2--WO_3-g-C_3N_4 electrode exhibits poor cycle performance attributed to the chemical and structural shortcomings.

Comparatively, SnO_2-WO_3-g-C_3N_4 nanocomposite from the current work was superior to most recently reported ternary composites with SnO_2, WO_3 and other carbonaceous materials (Table 3). Furthermore, WO_3-g-C_3N_4 displayed comparable C_s retention after similar cycles; however, SnO_2-WO_3-g-C_3N_4 and SnO_2-g-C_3N_4 were lower. In addition, SnO_2-g-C_3N_4 in the current study was inferior to that reported by Xu et al. [47] and this could be attributed to different electrolyte systems and synthesis protocols.

4. Conclusions

In the drive to enhance energy storage capabilities, the study demonstrated that binary and ternary nanocomposites containing SnO_2 and WO_3 synergistically and favourably modified g-C_3N_4 for supercapacitor applications using a straightforward hydrothermal synthesis protocol. Among other physicochemical properties tailored in the current nanocomposites are surface area, morphology, crystallinity, and mechanical stability. For example, the SnO_2-g-C_3N_4 binary nanocomposite and SnO_2-WO_3-g-C_3N_4 ternary nanocomposite improved the BET surface area by 160 % and 133 %, respectively. The charge

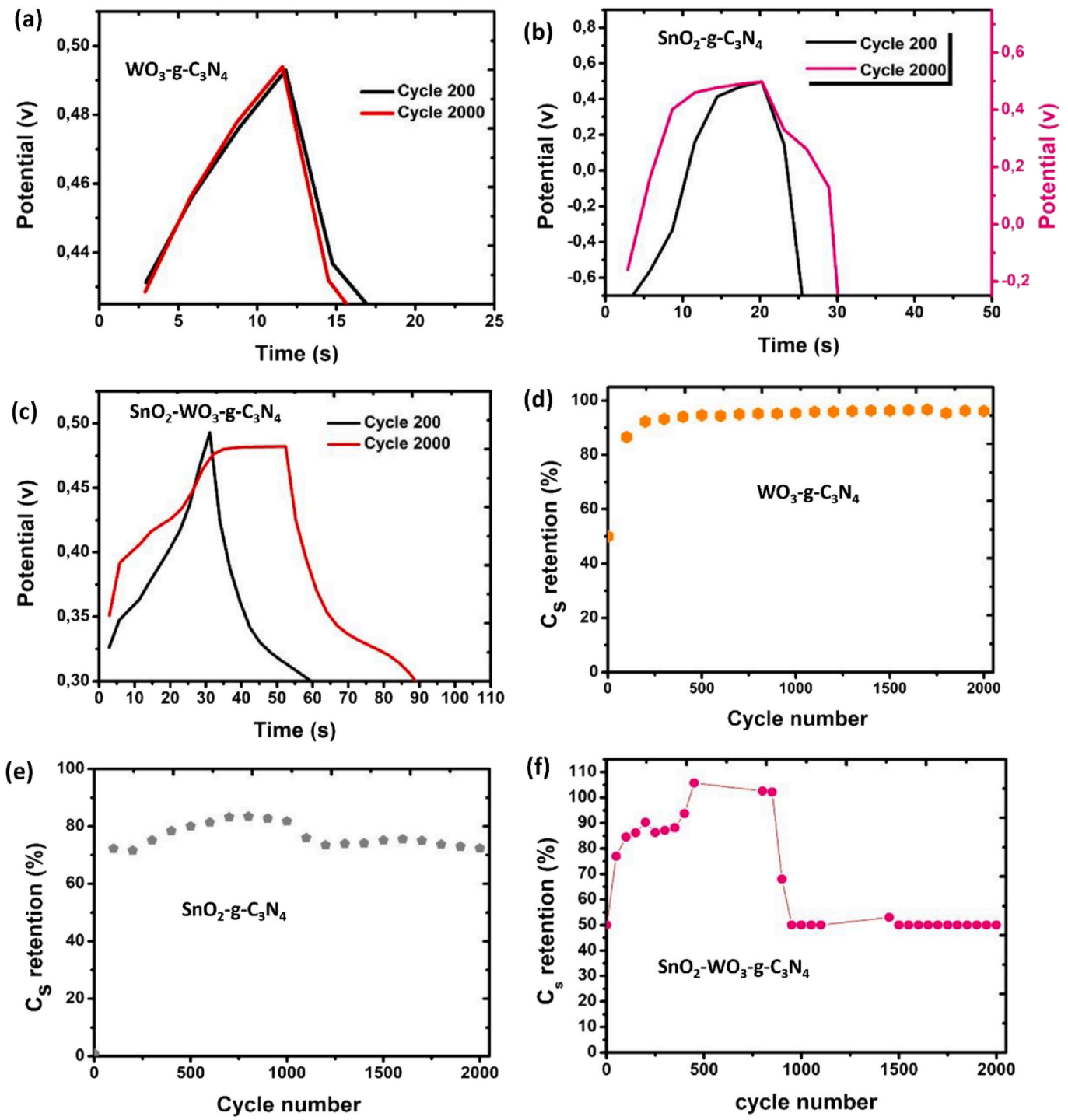

Fig. 10. The GCD curves compared at 200th and 2000th cycles of (a) WO_3-g-C_3N_4, (b) SnO_2-g-C_3N_4 and (c) SnO_2-WO_3-g-C_3N_4, and cyclic stability studies of for (d) WO_3-g-C_3N_4, (e) SnO_2-g-C_3N_4 and (f) SnO_2-WO_3-g-C_3N_4.

transport resistance was reduced to 63 % and 38 % of that of g-C_3N_4 electrodes in the SnO_2-g-C_3N_4 and WO_3-g-C_3N_4 binary nanocomposites, respectively. Furthermore, this tailoring led to enhanced energy storage performance, such as the impressive 96 % capacitance retention after 2000 cycles achieved with the WO_3-g-C_3N_4 binary nanocomposite. Additionally, the specific capacitance of g-C_3N_4 electrodes increased by 119 %, 172 %, and 192 % in the SnO_2-g-C_3N_4 and WO_3-g-C_3N_4 binary nanocomposites and the SnO_2-WO_3-g-C_3N_4 ternary nanocomposite, respectively. Consequently, the transformed morphology and synergism with other physicochemical properties of the g-C_3N_4 nanocomposites in the current study effectively buffered volume expansion and enhanced the conductivity of the components to achieve superior electrochemical properties. In summary, the study illustrated the feasibility of advancing the energy storage characteristics of g-C_3N_4 through nanocomposites with SnO_2 and WO_3. This approach is well-suited for emerging solid-state and photo-assisted supercapacitors as a sustainable pathway to new materials.

Table 3
Comparison of the synthesised nanocomposites with other recent carbon-based nanocomposites.

Material	Electrolyte	% C_s improvement	% C_s retention	Reference
SnO_2-g-C_3N_4	1 M H_2SO_4	600	97 @ 5000	[47]
SnO_2 quantum dots (QDs)-rGO	1 M Na_2SO_4	266	96@ 6000	[48]
SnO_2–C beads	1 M KOH	1234	96@ 6000	[49]
$WO_3(H_2O)_{0.33}$-g-C_3N_4	1 M KOH	330	99@ 10000	[50]
WO_3-rGO	1 M H_2SO_4	170	93 @ 2000	[17]
WO_3-MWCNT	0.5 M H_2SO_4	163	80@ 4000	[51]
Zn_2SnO_4–SnO_2-CNT	6 M KOH	157	93 @ 15000	[52]
SnO_2 QDs-GO-polypyrrole	3 M KOH	126	–	[53]
monoclinic-WO_3-$Ti_3C_2T_X$-hollow graphene foam	1 M H_2SO_4	138	93@ 5000	[24]
WO_3-WS_2-MWCNTs	3 M KOH	127	95@ 5000	[23]
WO_3-g-C_3N_4	2 M KOH	172	96 @ 2000	This work
SnO_2-g-C_3N_4		119	70 @ 2000	
SnO_2-WO_3-g-C_3N_4		192	50 @ 2000	

CRediT authorship contribution statement

Peter Kganyago: Writing – original draft, Methodology, Investigation, Formal analysis, Conceptualization. **Messai Mamo:** Writing – review & editing, Validation, Supervision, Formal analysis, Conceptualization. **Edwin T. Mombeshora:** Writing – review & editing, Validation, Formal analysis, Data curation. **Patrick G. Ndungu:** Writing – review & editing, Validation, Supervision, Project administration, Methodology, Funding acquisition, Conceptualization.

Funding details

This work was partially supported by the National Research Foundation of South Africa, the National Nanoscience Postgraduate Teaching and Training Platform (an initiative of the South African Department of Science and Innovation), the Faculty of Science at the University of Johannesburg, and by the Faculty of Natural and Agricultural Sciences at the University of Pretoria.

Declaration of competing interest

The authors declare that they have no known competing financial interests or personal relationships that could have appeared to influence the work reported in this paper.

Acknowledgements

PK is grateful to the National Nanoscience Postgraduate Teaching and Training Platform, funded by the South African Department of Science and Innovation, for bursary support. ETM thanks the University of Pretoria Research Development Fund. The authors acknowledge the Faculty of Science at the University of Johannesburg and the Faculty of Natural and Agricultural Sciences at the University of Pretoria for research support.

Appendix A. Supplementary data

Supplementary data to this article can be found online at https://doi.org/10.1016/j.matchemphys.2025.131566.

Data availability

Data will be made available on request.

References

[1] F. Li, Y. Dong, Q. Dai, T.T. Nguyen, M. Guo, Novel freestanding core-shell nanofibrillated cellulose/polypyrrole/tubular graphitic carbon nitride composite film for supercapacitors electrodes, Vacuum 161 (2019) 283–290.
[2] E.T. Mombeshora, E. Muchuweni, H. Hashemi, Applications of graphene derivatives in all-solid-state supercapacitors, ChemistrySelect 9 (2024) e202404345.
[3] M. Ghaemmaghami, R. Mohammadi, Carbon nitride as a new way to facilitate the next generation of carbon-based supercapacitors, Sustain. Energy Fuels 3 (2019) 2176–2204.
[4] D. Guo, J. Qian, R. Xin, Z. Zhang, W. Jiang, G. Hu, M. Fan, Facile synthesis of nitrogen-enriched nanoporous carbon materials for high performance supercapacitors, J. Colloid Interface Sci. 538 (2019) 199–208.
[5] E.T. Mombeshora, E. Muchuweni, The current impacts and future prospects of graphene derivatives in polymer-based supercapacitors, Discov. Mater. 3 (2023) 32.
[6] E.T. Mombeshora, E. Muchuweni, M.L. Davies, B.S. Martincigh, V.O. Nyamori, Nitrogen-doped reduced graphene oxide-polyaniline composite materials: hydrothermal treatment, characterisation and supercapacitive properties, Nouv. J. Chim. 47 (2023) 3502–3515.
[7] S. Khan, S. Gouadria, A.G. Al-Sehemi, A. Kumar, Synthesis of an effective iron manganese oxide-cobalt oxide nanocomposite electrode for energy storage supercapacitors, Ceram. Int. 51 (2025) 36054–36063.
[8] K. Mugadza, E.T. Mombeshora, A. Stark, P.G. Ndungu, V.O. Nyamori, Surface modifications of carbon nanotubes towards tailored electrochemical characteristics, J. Mater. Sci. Mater. Electron. 32 (2021) 27923–27936.
[9] N.S. Lopa, M.K. Akbari, D. Wu, F. Verpoort, S. Zhuiykov, Two-dimensional SnO_2-ZnO nanohybrid electrode fabricated via atomic layer deposition for electrochemical supercapacitors, Energ. Fuel. 37 (2023) 3142–3151.
[10] E.T. Mombeshora, E. Muchuweni, M.L. Davies, V.O. Nyamori, B.S. Martincigh, Electrochemical capacitors: basic concepts and emerging nanomaterials for electrodes, in: N.V. Kulkarni, B.I. Kharissov (Eds.), Handbook of Emerging Materials for Sustainable Materials for Energy, Elsevier, 2024, pp. 83–118.
[11] N.D. Raskar, D.V. Dake, V.A. Mane, R.B. Sonpir, V.D. Mote, M. Vasundhara, P. C. Zine, M.D. Shirsat, K.P. Gattu, B.N. Dole, MXene/Tungsten-Functionalized graphene oxide nanosheets as conductive platforms for feni-co-doped MnO_2 nanocomposites: toward high-performance supercapacitor electrodes, Solid State Sci. 166 (2025) 107974.
[12] M. Elshafie, S.A. Younis, P. Serp, E.A.M. Gad, Preparation characterization and non-isothermal decomposition kinetics of different carbon nitride sheets, Egypt. J. Pet. 29 (2020) 21–29.
[13] A. Ibrahim, U.B. Memon, S.P. Duttagupta, I. Mahesh, R.K.S. Raman, A. Sarkar, G. Pendharkar, S.S.V. Tatiparti, Nano-structured palladium impregnate graphitic carbon nitride composite for efficient hydrogen gas sensing, Int. J. Hydrogen Energy 45 (2020) 10623–10636.
[14] E.O. Oseghe, S.O. Akpotu, E.T. Mombeshora, A.O. Oladipo, L.M. Ombaka, B. B. Maria, A.O. Idris, G. Mamba, L. Ndlwana, O.S. Ayanda, A.E. Ofomaja, V. O. Nyamori, U. Feleni, T.T.I. Nkambule, T.A.M. Msagati, B.B. Mamba, D. W. Bahnemann, Multi-dimensional applications of graphitic carbon nitride nanomaterials – a review, J. Mol. Liq. 344 (2021) 117820.
[15] M. Chegeni, Z. Mousavi, M. Soleymani, S. Dehdashtian, Removal of aspirin from aqueous solutions using graphitic carbon nitride nanosheet: theoretical and experimental studies, Diam. Relat. Mater. 101 (2020) 107621.
[16] G. Mineo, E. Bruno, S. Mirabella, Advances in WO_3-based supercapacitors: state-Of-the-art research and future perspectives, Nanomaterials (Basel) 13 (2023) 1418.
[17] P. Bhojane, P.M. Shirage, Facile preparation of hexagonal WO_3 nanopillars and its reduced graphene oxide nanocomposites for high-performance supercapacitor, J. Energy Storage 55 (2022) 105649.
[18] M. Faraji, R. Khalilzadeh Soltanahmadi, H. Mohammadzadeh Aydisheh, B. Mostafavi Bavani, 2.0-V flexible all-solid-state symmetric supercapacitor device with high electrochemical performance composed of MWCNTs-WO_3-graphite sheet, Ionics 26 (2020) 3003–3013.
[19] M.M. Momeni, Z. Yazdani, H.M. Aydisheh, Light-assisted supercapacitors based on CNT-WO_3 hybrid dual photoelectrodes, J. Alloys Compd. 1031 (2025) 180973.
[20] P.A. Shinde, Y. Seo, C. Ray, S.C. Jun, Direct growth of WO_3 nanostructures on multi-walled carbon nanotubes for high-performance flexible all-solid-state asymmetric supercapacitor, Electrochim. Acta 308 (2019) 231–242.
[21] D. Li, J. Lin, Y. Lu, Y. Huang, X. He, C. Yu, J. Zhang, C. Tang, MnO_2 nanosheets grown on N-doped agaric-derived three-dimensional porous carbon for asymmetric supercapacitors, J. Alloys Compd. 815 (2020) 152344.
[22] S.B. Patil, R.P. Nikam, V.C. Lokhande, C.D. Lokhande, R.S. Patil, Tungsten oxide/reduced graphene oxide composite electrodes for solid-state asymmetric supercapacitor application, ACHM 8 (2025) 175.
[23] J. Aftab, S. Mehmood, A. Ali, I. Ahmad, M.F. Bhopal, M.Z.U. Rehman, M.Z.U. Shah, A.U. Shah, M. Wang, M.F. Khan, A.S. Bhatti, Synergetic electrochemical performance of tungsten oxide/tungsten disulfide/MWCNTs for high-performance aqueous asymmetric supercapattery devices, J. Alloys Compd. 965 (2023) 171366.

[24] A.M. Patil, J. Wang, S. Li, X. Hao, X. Du, Z. Wang, X. Hao, A. Abudula, G. Guan, Bilateral growth of monoclinic WO_3 and 2D $Ti_3C_2T_x$ on 3D free-standing hollow graphene foam for all-solid-state supercapacitor, Chem. Eng. J. 421 (2021) 127883.
[25] H. Huang, X. Ju, H. Li, B. Qu, T. Wang, Construction of complex WO_3-SnO_2 hollow nanospheres as a high-performance anode for lithium-ion batteries, J. Alloys Compd. 744 (2018) 375–380.
[26] K. Saravanakumar, J. Prasath, R. Rajesh, Synthesis of SnO_2 and MoS_2 nano composites for supercapacitor applications, Mater. Today Proc. 46 (2021) 8189–8195.
[27] X. Ren, Y. Liu, H. Sun, Z. Zhang, C. Luo, Y. Wang, C. Xu, H. Chen, One-step synthesis of SnS_2/SnO_2 nanoflowers for high-performance hybrid supercapacitors, J. Energy Storage 74 (2023) 109372.
[28] G. Zamiri, A. Haseeb, P. Jagadish, M. Khalid, I. Kong, S.G. Krishnan, Three-dimensional graphene-TiO_2-SnO_2 ternary nanocomposites for high-performance asymmetric supercapacitors, ACS Omega 7 (2022) 43981–43991.
[29] Z. Li, C. Zhang, J. Bu, L. Zhang, L. Cheng, M. Wu, Constructing a novel carbon skeleton to anchor Sn/SnO_2 nanodots for flexible supercapacitor with excellent rate capability, Carbon 194 (2022) 197–206.
[30] W. Pholauyphon, P. Charoen-amornkitt, T. Suzuki, S. Tsushima, Perspectives on accurately analyzing cyclic voltammograms for surface- and diffusion-controlled contributions, Electrochem. Commun. 159 (2024) 107654.
[31] P. Praus, L. Svoboda, M. Ritz, I. Troppová, M. Šihor, K. Kočí, Graphitic carbon nitride: synthesis, characterization and photocatalytic decomposition of nitrous oxide, Mater. Chem. Phys. 193 (2017) 438–446.
[32] M. Li, B. Wang, X. An, Z. Li, H. Zhu, B. Mao, D.G. Calatayud, T.D. James, A practical graphitic carbon nitride (g-C_3N_4) based fluorescence sensor for the competitive detection of trithiocyanuric acid and mercury ions, Dyes Pigments 170 (2019) 107476.
[33] D. Sandil, S. Srivastava, B.D. Malhotra, S.C. Sharma, N.K. Puri, Biofunctionalized tungsten trioxide-reduced graphene oxide nanocomposites for sensitive electrochemical immunosensing of cardiac biomarker, J. Alloys Compd. 763 (2018) 102–110.
[34] S. Samanta, R. Srivastava, A novel method to introduce acidic and basic bi-functional sites in graphitic carbon nitride for sustainable catalysis: cycloaddition, esterification, and transesterification reactions, Energ. Fuel. 1 (2017) 1390–1404.
[35] M. Inagaki, T. Tsumura, T. Kinumoto, M. Toyoda, Graphitic carbon nitrides (g-C_3N_4) with comparative discussion to carbon materials, Carbon 141 (2019) 580–607.
[36] L. Cao, P. Dai, L. Zhu, L. Yan, R. Chen, D. Liu, X. Gu, L. Li, Q. Xue, X. Zhao, Graphitic carbon nitride catalyzes selective oxidative dehydrogenation of propane, Appl. Catal. B Environ. 262 (2020) 118277.
[37] K. Maliutina, A. Tahmasebi, J. Yu, Effects of pressure on morphology and structure of bio-char from pressurized entrained-flow pyrolysis of microalgae, DIB 18 (2018) 422–431.
[38] L. Gao, F. Qu, X. Wu, Hierarchical WO_3@SnO_2core–shell nanowire arrays on carbon cloth: a new class of anode for high-performance lithium-ion batteries, J. Mater. Chem. A 2 (2014) 7367–7372.
[39] N. Hellgren, R.T. Haasch, S. Schmidt, L. Hultman, I. Petrov, Interpretation of X-ray photoelectron spectra of carbon-nitride thin films: new insights from in situ XPS, Carbon 108 (2016) 242–252.
[40] H.-J. Lee, A. Abdellah, F.M. Ismail, C. Gumeci, N. Dale, J. Parrondo, D.C. Higgins, Understanding the impact of nitrogen doping and/or amine functionalization of reduced graphene oxide via hydrothermal routes for supercapacitor applications, Electrochim. Acta 397 (2021) 139241.
[41] X. He, Z. Wu, Y. Xue, Z. Gao, X. Yang, Fabrication of interlayer beta-CD/g-C_3N_4@MoS_2 for highly enhanced photodegradation of glyphosate under simulated sunlight irradiation, RSC Adv. 9 (2019) 4635–4643.
[42] H. Lin, Y. Liu, J. Deng, S. Xie, X. Zhao, J. Yang, K. Zhang, Z. Han, H. Dai, Graphitic carbon nitride-supported iron oxides: High-performance photocatalysts for the visible-light-driven degradation of 4-nitrophenol, J. Photochem. Photobiol. Chem. 336 (2017) 105–114.
[43] J. Lin, X. Du, High performance asymmetric supercapacitor based on hierarchical carbon cloth in situ deposited with h-WO_3 nanobelts as negative electrode and carbon nanotubes as positive electrode, Micromachines 12 (2021) 1195.
[44] E.T. Mombeshora, R. Simoyi, V.O. Nyamori, P.G. Ndungu, Multiwalled carbon nanotube-titania nanocomposites: understanding nano-structural parameters and functionality in dye-sensitized solar cells, SAJChem 68 (2015).
[45] X. Zhu, J. Zhu, J. Wang, Z. Gan, G. Li, C. Meng, Experimental study on long cycling performance of NCM523 lithium-ion batteries and pptimization of charge-discharge strategy, J. Therm. Sci. 29 (2020) 1180–1192.
[46] Y. Wu, G. Gao, G. Wu, Self-assembled three-dimensional hierarchical porous V_2O_5/graphene hybrid aerogels for supercapacitors with high energy density and long cycle life, J. Mater. Chem. A 3 (2015) 1828–1832.
[47] Y. Xu, L. Wang, Y. Zhou, J. Guo, S. Zhang, Y. Lu, Synthesis of heterostructure SnO_2/graphitic carbon nitride composite for high-performance electrochemical supercapacitor, J. Electroanal. Chem. 852 (2019) 113507.
[48] Z. Wei, M. Liu, H. Li, S. Sun, L. Yang, SnO_2 quantum dots decorated reduced graphene oxide nanosheets composites for electrochemical supercapacitor applications, Int. J. Electrochem. Sci. 15 (2020) 6257–6268.
[49] M.U. Rani, V. Naresh, D. Damodar, S. Muduli, S.K. Martha, A.S. Deshpande, In-situ formation of mesoporous SnO_2@C nanocomposite electrode for supercapacitors, Electrochimic, Acta 365 (2021) 137284.
[50] G. Koyyada, B.S. Goud, M. Ouladsmane, J.H. Kim, N.H. Nguyen Thi, N.N. Dang, g-C_3N_4/$WO_3(H_2O)_{0.33}$ nanostructured electrode for hybrid asymmetric-supercapacitor, Ceram. Int. 49 (2023) 35837–35846.
[51] P.O. Anikpa, A.U. Mee, A.C. Nwanya, A.C. Nkele, D.B. Malavekar, R.U. Osuji, N. Nwulu, C.D. Lokhande, F.I. Ezema, Asymmetric supercapacitor performance of hydrothermally-synthesized MWCNT-WO_3 composite electrode, J. Energy Storage 81 (2024) 110439.
[52] E. Samuel, T.-G. Kim, C.-W. Park, B. Joshi, M.T. Swihart, S.S. Yoon, Supersonically sprayed Zn_2SnO_4/SnO_2/CNT nanocomposites for high-performance supercapacitor electrodes, ACS Sustain. Chem. Eng. 7 (2019) 14031–14040.
[53] M. Vandana, S. Veeresh, H. Ganesh, Y.S. Nagaraju, H. Vijeth, M. Basappa, H. Devendrappa, Graphene oxide decorated SnO_2 quantum dots/polypyrrole ternary composites towards symmetric supercapacitor application, J. Energy Storage 46 (2022) 103904.